

# Novel discretization strategies for the 2D non-Newtonian resistance term in geophysical shallow flows

S. Martínez-Aranda<sup>\*</sup>, J. Murillo, M. Morales-Hernández, P. García-Navarro

*Fluid Dynamic Technologies – I3A, University of Zaragoza, Zaragoza, Spain*



## ARTICLE INFO

**Keywords:**  
 Geophysical shallow flows  
 Non-Newtonian rheological models  
 2D resistance integration  
 Explicit upwind  
 Implicit centered  
 Rotational invariance

## ABSTRACT

In the context of two-dimensional models for complex geophysical surface flows such as debris flows, muddy slurries, oil spills over land, hyperconcentrated floods, lava flows, etc, depth-averaged rheological models relate the shear stress state within the fluid column to the depth-averaged local flow features. Despite it is the most influencing term on the mobility of complex shallow flows, the numerical treatment of the resistance contribution to the flow momentum is still a challenging topic, especially when dealing with 2D large-scale applications. In this work, two novel strategies for the explicit upwind discretization of generalized non-Newtonian resistance terms in two-dimensional numerical models are proposed, called integral and differential approaches. These new strategies are applicable to generalized rheological formulations in any type of mesh topology. Results from benchmark tests running in orthogonal, triangle structured and triangle unstructured meshes demonstrate that both approaches represent an improvement for the explicit upwind integration of the 2D resistance force compared with previous procedures. It is shown that the alignment of the flow with the mesh main-axis, which has been previously attributed to faults of 2D FV numerical methods and insufficient mesh refinements, is directly related to the loss of the rotational invariance of the integrated resistance force. This is caused by the erroneous procedure for including the 2D resistance term into the local flux balance at the cell edges. Furthermore, a novel implicit centered method for the integration of the 2D resistance force has also been derived for the quadratic frictional non-linear resistance formulation. Despite the implicit procedure fails to converge to steady uniform flow states, the differential explicit upwind and the implicit centered methods show similar level of accuracy, robustness and computational efficiency for transient 2D frictional visco-plastic flows.

## 1. Introduction

In the context of depth-averaged two-dimensional models for geophysical surface flows, the resistance of the fluid to motion is incorporated into the 2D momentum equations using rheological models which relate the shear stress state within the fluid column to the depth-averaged local flow features. Rheological models for complex shallow flows are usually non-Newtonian relations derived under the simple-shear assumption including stop & go mechanism (Quecedo et al., 2004; Pastor et al., 2015) or semi-empirical formulations based on steady laboratory experiments (Naef et al., 2006; Murillo and García-Navarro, 2012). The mathematical modeling of complex unsteady phenomena, such as realistic debris flows, muddy slurries, oil spills over land, hyperconcentrated floods or lava flows, and their numerical resolution is still a challenging topic, especially when dealing with large-scale and long-term applications (Martínez-Aranda et al., 2021).

Despite it is the most influencing term on the movement of complex shallow flows, the numerical treatment of the resistance source term has received historically less attention in literature than the integration of the flux derivatives or other source terms, such as the bed-pressure term (Rosatti et al., 2008). When dealing with non-Newtonian flows, the resistance term involves an increasing complexity derived from the non-linear relation between stress and shear rate. The non-Newtonian behavior leads to a more important influence of the resistance contribution in the numerical solution as the boundary shear stress magnitude grows. Moreover, under quiescent conditions, the basal resistance contribution may not be null due to the existence of a frictional/cohesive yield strength and the well-balanced behavior of the solution must be reexamined. To overcome these issues most of the numerical schemes reported in literature for non-Newtonian flows use cell-centered integration techniques for the discretization of the shear resistance (Ouyang et al., 2015; George and Iverson, 2014; Luna et al., 2012; Armanini et al.,

\* Corresponding author.

E-mail address: [sermar@unizar.es](mailto:sermar@unizar.es) (S. Martínez-Aranda).

2009; Xia et al., 2017). This ensures that the integrated resistance force satisfies the property of invariance under rotation (Godlewski and Raviart, 1996a; Toro, 1997) but requires implicit or semi-implicit resolution to gain stability (Xia et al., 2018; Li et al., 2018) and is not easily applicable to all the non-Newtonian rheological models. Trying to take advantage of the implicit computation of the resistance term but avoiding iterative methods, some procedures have been developed for the quadratic turbulent Newtonian friction in 1D and 2D shallow water models (Burguete et al., 2008; Xia and Liang, 2018; Brufau et al., 2000; Cea and Bladé, 2015).

The explicit integration of the basal resistance term offers a higher flexibility since it can be applied to any non-Newtonian rheological model (Murillo and García-Navarro, 2012; Juez and Murillo, 2013). However, the explicit integration requires a careful treatment in order to avoid numerical instabilities and additional time step restrictions even using the common hydraulic resistance formulations based on the turbulent Newtonian shearing model (Burguete et al., 2008; Murillo et al., 2008). These additional time step restrictions can lead to a marked increase of the computational time required by the model. The consequence is a reduction of the efficiency, regardless of how the scheme is implemented (programming language, parallel computing, available hardware, etc). The explicit upwind discretization of the resistance term at the cell edges based on the Roe Riemann solver helps to improve the stability and well-balanced character of the explicit numerical solution, regardless of the resistance model considered (Murillo and Navas-Montilla, 2016; Martínez-Aranda et al., 2020). Furthermore, the spatial discretization of the basal resistance force in the 2D framework is open to different possibilities since, contrarily to bed-pressure momentum source contribution, the maintenance of the rotation invariant property is not straightforward for the 2D shear stresses (Cozzolino et al., 2021). The development of new numerical procedures which avoid the dependence of the integrated resistance force on the mesh topology in the 2D framework is a key point in the development of Efficient Simulation Tools (EST) for geophysical surface flows (Martínez-Aranda et al., in press, 2021).

In this work, two novel approaches for the explicit upwind discretization of generalized non-Newtonian resistance terms in two-dimensional numerical models are proposed and compared with the classical procedure. Furthermore, based on the development of Xia and Liang (2018) for pure turbulent flows, an additional novel non-iterative implicit method is proposed for the cell-centered computation of resistance force and compared with the explicit techniques in terms of robustness, accuracy and computational efficiency. The equation system is here particularized for mud/debris shallow flows but the proposed resistance integration procedures are applicable to any kind of hyperbolic geophysical flow. The paper is structured as follows: Section 2 is devoted to the governing equation for compressible mud/debris flows; the first-order Finite Volume (FV) method for generalized mesh topology is introduced in Section 3; the novel integral and differential explicit upwind methods for generalized resistance are presented in Section 4, as well as the classical approach for completeness; Section 5 is devoted to the novel implicit procedure for the quadratic frictional non-linear resistance; in Section 6 the explicit and implicit integration procedures have been faced to 1D and 2D benchmark tests in order to analyse their behaviour in terms of accuracy, robustness and efficiency; and the main conclusions are drawn in Section 7. Finally, three additional appendixes have been included: Appendix A includes the derivation of the depth-averaged models for the basal resistance terms in the momentum equations, Appendix B details the computation of the frictionless flux at the cell edges based on the Roe strategy and Appendix C is devoted to the derivation of the implicit integration procedure for quadratic frictional resistance.

## 2. Governing equations

The depth-averaged 2D model for the variable-density multi-grain

mixture flows (Martínez-Aranda et al., 2021) involves the continuity equations for the liquid-solid mixture mass

$$\frac{\partial(\rho h)}{\partial t} + \frac{\partial}{\partial x}(\rho hu) + \frac{\partial}{\partial y}(\rho hv) = 0 \quad (1)$$

and the conservation laws of the bulk linear momentum along the  $x$ - and  $y$ - coordinates expressed as

$$\frac{\partial(\rho hu)}{\partial t} + \frac{\partial}{\partial x}(\rho hu^2 + \frac{1}{2}g\rho h^2) + \frac{\partial}{\partial y}(\rho hvu) = -g\rho h \frac{\partial z_b}{\partial x} - \tau_{bx} \quad (2a)$$

$$\frac{\partial(\rho hv)}{\partial t} + \frac{\partial}{\partial x}(\rho hvu) + \frac{\partial}{\partial y}(\rho hv^2 + \frac{1}{2}g\rho h^2) = -g\rho h \frac{\partial z_b}{\partial y} - \tau_{by} \quad (2b)$$

being  $\rho$  the depth-averaged bulk density,  $h$  the vertical flow depth and  $(u, v)$  the components of the depth-averaged flow velocity vector  $\mathbf{u}$ ,  $z_b$  the bed layer elevation,  $(\tau_{bx}, \tau_{by})$  the components of the depth-averaged basal resistance vector  $\boldsymbol{\tau}_b$  and  $g$  the gravitational acceleration.

The bulk mixture density  $\rho$  in the flow column is expressed as

$$\rho = \rho_w + (\rho_s - \rho_w) \phi \quad (3)$$

where  $\rho_w$  is the pore-water density, and  $\rho_s$  and  $\phi$  are the density and depth-averaged volumetric concentration of the solid phase in the flow column.

The depth-averaged transport equations for the solid phase reads

$$\frac{\partial(h\phi)}{\partial t} + \frac{\partial}{\partial x}(hu\phi) + \frac{\partial}{\partial y}(hv\phi) = 0 \quad (4)$$

Fig. 1 shows an sketch with the main variables involved in the system of equations used for modelling variable-density water-sediment mixture flows over fixed beds. It is worth noting that the entrainment/deposition net flux on the right hand side of (1) and (4) has been neglected. This mass exchange term is relevant in sediment-laden flows and must be included in realistic long-term applications. However, this work is specifically focused on the effects of the 2D basal resistance discretization and the inclusion of the entrainment/deposition flux generates density gradients and topographical changes which can hide the actual effects of the correct/erroneous discretization procedure in the numerical results.

The basal shear stress vector in the momentum Eqs. (2a) is expressed as

$$\boldsymbol{\tau}_b = (\tau_{bx}, \tau_{by}) = \tau_b \mathbf{n}_u \quad (5)$$

being  $\tau_b$  the basal shear stress modulus and  $\mathbf{n}_u = (n_{ux}, n_{uy})$  the velocity unit vector.

To close the depth-averaged basal resistance term, two different widespread formulations are considered in this work (Pastor et al., 2015;

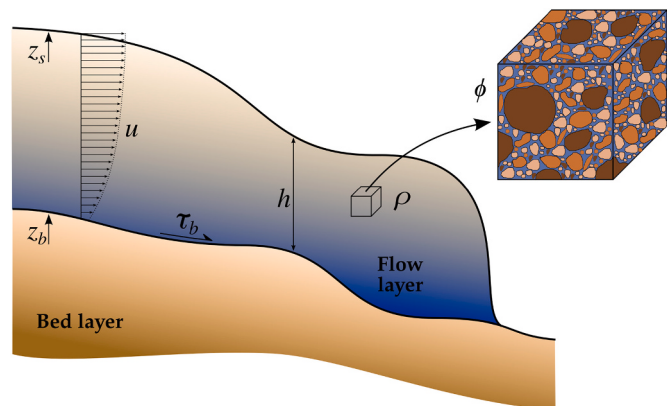


**Fig. 1.** Main variables involved in a sediment-laden flow.

[Martínez-Aranda, 2021](#)). First, for cohesive linear visco-plastic behaviour (Fig. 2a), the Bingham model relates the basal shear stress modulus  $\tau_b$ , the cohesive yield strength  $\tau_y$  [Pa] and the averaged flow velocity  $\mathbf{u}$  using the cubic equation

$$2\tau_b^3 - 3\left(\tau_y + 2\mu_B \frac{|\mathbf{u}|}{h}\right)\tau_b^2 + \tau_y^3 = 0 \quad (6)$$

being  $\mu_B$  [Pa·s] the dynamic viscosity of the fluid. Second, the Herschel-Bulkley model is used for modelling the basal stress  $\tau_b$  in non-linear visco-plastic flows with a frictional-type yield strength  $\tau_f$  [Pa] as

$$\tau_b = \tau_f + \left(\frac{2m+1}{m}\right)^m \mu_p \left(\frac{|\mathbf{u}|}{h}\right)^m \quad (7)$$

being  $m$  the behaviour index of the fluidized material and  $\mu_p$  [Pa·s<sup>m</sup>] the plastic viscosity. The frictional yield strength  $\tau_f$  is calculated here using the Coulomb-type relation

$$\tau_f = (\rho - \rho_w) g \operatorname{htan} \delta_f \quad (8)$$

where  $\delta_f$  is the basal frictional angle for the solid phase. The detailed derivation of the depth-averaged Bingham and frictional Herschel-Bulkley models for the basal resistance has been included in [Appendix A](#).

It is worth mentioning that (7) represents a generalized depth-integrated formulation for frictional visco-plastic flows which encompasses from shear-thinning behavior for  $m < 1$ , reducing the apparent viscosity as the induced shear rate increases, to shear-thickening behaviour for  $m > 1$ , increasing the apparent viscosity as the induced shear rate grows (Fig. 2b). Furthermore, if the viscous momentum dissipation is neglected, expression (7) reduces to the Coulomb-Terzaghi model  $\tau_b = (\rho - \rho_w) g \operatorname{htan} \delta_f$  ([Coulomb, 1773](#); [Terzaghi, 1936](#)), widely used for estimating frictional shear stresses in flows of saturated granular masses ([Iverson and Vallance, 2001](#); [Lancaster et al., 2003](#); [Jakob and Hungr, 2005](#); [Iverson et al., 2010](#)).

The resulting system is composed by four conservation equations accounting for the mixture flow (1)–(2a)–(2b) and the transport of the solid phase (4). Considering that the density of the fluid-solid mixture follows the relation (3), the dimensionless bulk density  $r$  can be expressed by defining a new variable  $\phi'$ , referred to as buoyant solid concentration, as

$$r = \frac{\rho}{\rho_w} = 1 + \phi' \quad \text{with } \phi' = \frac{\rho_s - \rho_w}{\rho_w} \phi \quad (9)$$

Using (9), the equations forming the system can be recast in vector form as

$$\frac{\partial \mathbf{U}}{\partial t} + \nabla \cdot \mathbf{E}(\mathbf{U}) = \mathbf{S}_b(\mathbf{U}) + \mathbf{S}_\tau(\mathbf{U}) \quad (10)$$

where  $\mathbf{U}$  is the vector of conserved variables

$$\mathbf{U} = (rh, rhu, rhv, h\phi')^T \quad (11)$$

and  $\mathbf{E}(\mathbf{U}) = (\mathbf{F}(\mathbf{U}), \mathbf{G}(\mathbf{U}))$  are the convective fluxes along the  $\mathbf{X} = (x, y)$  horizontal coordinates

$$\mathbf{F}(\mathbf{U}) = \begin{pmatrix} rhu \\ rhu^2 + \frac{1}{2}g rh^2 \\ rhuv \\ hu \phi' \end{pmatrix} \quad \mathbf{G}(\mathbf{U}) = \begin{pmatrix} rhv \\ rhuv \\ rhv^2 + \frac{1}{2}g rh^2 \\ hv \phi' \end{pmatrix} \quad (12)$$

It is worth noting that the dimensionless mixture density  $r$  and flow features  $(h, u, v)$  are coupled in the conserved variables and convective fluxes on the left hand side of (10).

The vector  $\mathbf{S}_b(\mathbf{U})$  accounts for the momentum source term associated to the variation of the pressure force on the bed interface, whereas  $\mathbf{S}_\tau(\mathbf{U})$  is the momentum dissipation due to the basal resistance.

$$\mathbf{S}_b(\mathbf{U}) = \begin{pmatrix} 0 \\ -g rh \frac{\partial z_b}{\partial x} \\ -g rh \frac{\partial z_b}{\partial y} \\ 0 \end{pmatrix} \quad \mathbf{S}_\tau(\mathbf{U}) = \begin{pmatrix} 0 \\ -\frac{\tau_b}{\rho_w} n_{ux} \\ -\frac{\tau_b}{\rho_w} n_{uy} \\ 0 \end{pmatrix} \quad (13)$$

This model is suitable for highly transient sediment-laden flows with noticeable density gradients, as occurs in densely-packed mud/debris flows over erodible steep beds ([Martínez-Aranda, 2021](#)).

### 3. Finite volume method for compressible shallow flows with source terms

This section is devoted to the derivation of the Finite Volume (FV) numerical scheme for 2D variable-density flow. System (10) is time dependent, non linear and contains momentum source terms. Under the hypothesis of dominant advection it can be classified as belonging to the family of hyperbolic systems. In order to obtain a numerical solution, the spatial domain is divided in computational cells using a fixed-in-time mesh and system (10) is integrated in each cell  $\Omega_i$ . Applying the Gauss theorem leads to

$$\frac{d}{dt} \int_{\Omega_i} \mathbf{U} d\Omega + \oint_{\partial\Omega_i} \mathbf{E}(\mathbf{U}) \cdot \mathbf{n} dl = \int_{\Omega_i} \mathbf{S}_b(\mathbf{U}) d\Omega + \int_{\Omega_i} \mathbf{S}_\tau(\mathbf{U}) d\Omega \quad (14)$$

being  $\mathbf{E}(\mathbf{U}) \cdot \mathbf{n}$  the normal flux and  $\mathbf{n}$  the outward unit normal vector along the  $i$  cell boundary  $\partial\Omega_i$ . Assuming a piecewise uniform representation of the conserved variables  $\mathbf{U}$  at the cell  $\Omega_i$ , the integrated system (14) can be expressed as

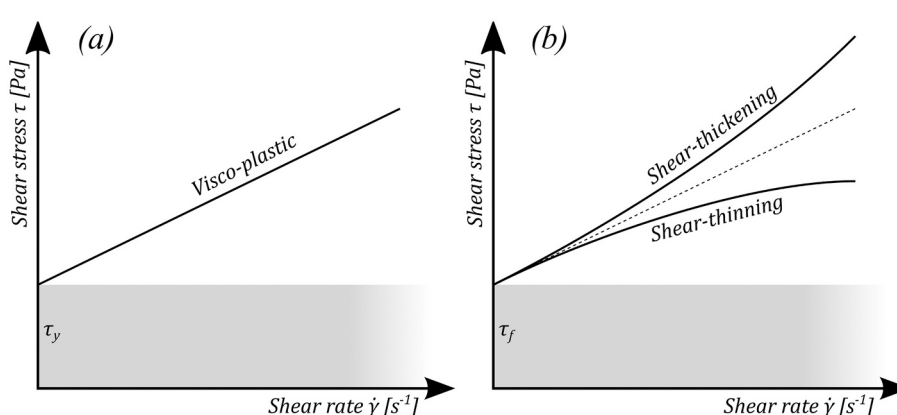


**Fig. 2.** Rheological behaviour for (a) the cohesive Bingham and (b) the frictional Herschel-Bulkley models.

$$\frac{d}{dt} \int_{\Omega_i} U \, d\Omega + \sum_{k=1}^{NE} (\mathbf{E} \cdot \mathbf{n})_k l_k = \int_{\Omega_i} S_b(U) \, d\Omega + \int_{\Omega_i} S_t(U) \, d\Omega \quad (15)$$

being  $NE$  the number of edges for the  $i$  cell,  $(\mathbf{E} \cdot \mathbf{n})_k$  the value of the normal flux through the  $k$ th edge,  $l_k$  the length of the edge (Fig. 3).

On the left hand side of (15), also called homogeneous part, the conservative flux matrix  $\mathbf{E}(U)$  satisfies the rotation invariant property (Godlewski and Raviart, 1996b) since

$$\nabla \cdot \mathbf{E}(U) = \mathbf{R}_k^{-1} \hat{\nabla} \cdot \mathbf{E}(\mathbf{R}_k U) \quad (16)$$

where  $\hat{\nabla} = \mathbf{R}_k \nabla$  and  $\mathbf{R}_k$  is a  $2 \times 2$  rotation matrix which projects the global orthogonal coordinates  $X = (x, y)$  into the local framework  $\hat{X} = \mathbf{R}_k X = (\hat{x}, \hat{y})$ , being  $\hat{x}$  and  $\hat{y}$  the normal and the tangential coordinate to the  $k$ th cell edge respectively (Fig. 4):

$$\mathbf{R}_k = \begin{pmatrix} \mathbf{n} \\ \mathbf{t} \end{pmatrix}_k = \begin{pmatrix} n_x & n_y \\ -n_y & n_x \end{pmatrix}_k \quad (17)$$

where  $\mathbf{n} = (n_x, n_y)$  and  $\mathbf{t} = (-n_y, n_x)$  are the normal and tangential unit vectors respectively. The complete  $4 \times 4$  rotation matrix  $\mathbf{R}_k$  in (16) and its inverse  $\mathbf{R}_k^{-1}$  for the  $k$ th cell edge are defined as

$$\mathbf{R}_k = \begin{pmatrix} 1 & & & \\ & \mathbf{R} & & \\ & & 1 & \\ & & & 1 \end{pmatrix}_k = \begin{pmatrix} 1 & 0 & 0 & 0 \\ 0 & n_x & n_y & 0 \\ 0 & -n_y & n_x & 0 \\ 0 & 0 & 0 & 1 \end{pmatrix}_k \quad (18)$$

$$\mathbf{R}_k^{-1} = \begin{pmatrix} 1 & & & \\ & \mathbf{R}^{-1} & & \\ & & 1 & \\ & & & 1 \end{pmatrix}_k = \begin{pmatrix} 1 & 0 & 0 & 0 \\ 0 & n_x & -n_y & 0 \\ 0 & n_y & n_x & 0 \\ 0 & 0 & 0 & 1 \end{pmatrix}_k$$

and the convective flux term in (15) satisfies the condition (Toro, 1997)

$$(\mathbf{E} \cdot \mathbf{n})_k = [F(U) n_x + G(U) n_y]_k = \mathbf{R}_k^{-1} F(\mathbf{R}_k U) \quad (19)$$

In order to develop 2D numerical schemes able to perform efficiently in unstructured meshes, the property (19) is used to express the homogeneous left hand side of (15) as

$$\frac{d}{dt} \int_{\Omega_i} U \, d\Omega + \sum_{k=1}^{NE} \mathbf{R}_k^{-1} F(\mathbf{R}_k U) l_k \quad (20)$$

where  $F(\mathbf{R}_k U)$  denotes the homogeneous normal flux vector through the  $k$ th cell edge expressed in the local framework  $\hat{X} = (\hat{x}, \hat{y})$ .

The set of local conservative variables  $\hat{U} \equiv \mathbf{R}_k U$  at the cell edge is defined as

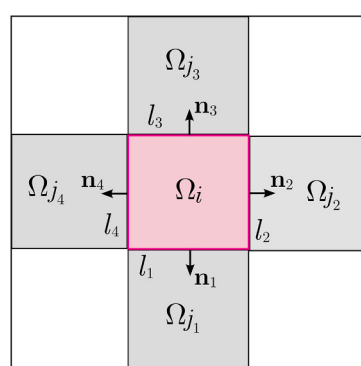


Fig. 3. Computational cells in (left) orthogonal and (right) triangular meshes.

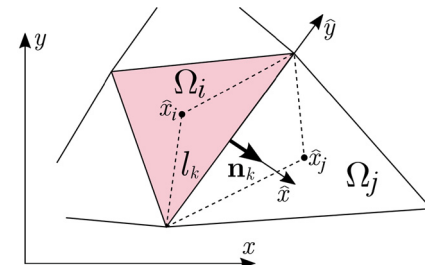


Fig. 4. Local coordinates at the  $k$ th cell edge.

$$\hat{U} \equiv \mathbf{R}_k U = (rh, rh u_n, rh v_t, h \phi^\chi)^T \quad (21)$$

where  $u_n = \mathbf{u} \cdot \mathbf{n} = u n_x + v n_y$  and  $v_t = \mathbf{u} \cdot \mathbf{t} = -u n_y + v n_x$  are the components of the flow velocity in the local framework, and the homogeneous flux vector  $F(\hat{U})_k \equiv F(\mathbf{R}_k U)$  is expressed as

$$F(\hat{U})_k \equiv F(\mathbf{R}_k U) = \begin{pmatrix} rh u_n \\ rh u_n^2 + \frac{1}{2} g rh^2 \\ rh u_n v_t \\ h u_n \phi^\chi \end{pmatrix}_k \quad (22)$$

The value of the fluxes through the  $k$ th cell edge can be augmented incorporating the non-conservative contribution of the bed-pressure term  $S_b$  into the homogeneous normal fluxes  $F(\hat{U})_k$  (Murillo and García-Navarro, 2010). The cell integral of the bed-pressure term  $S_b$  is unconditionally invariant under rotation (Castro et al., 2009; Murillo and Navas-Montilla, 2016) and can be split within the local framework  $\hat{X}$  of each edge using

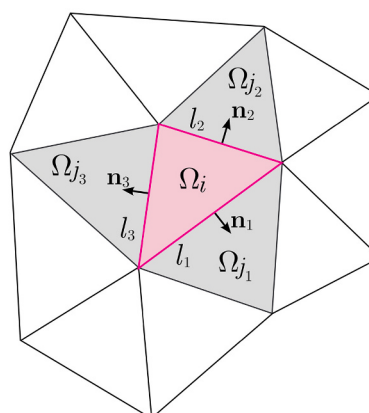
$$\int_{\Omega_i} S_b(U) \, d\Omega = \sum_{k=1}^{NE} \mathbf{R}_k^{-1} H(\hat{U})_k l_k \quad (23)$$

where  $H(\hat{U})_k = (0, -g rh \Delta z_b, 0, 0)_k^T$  is the integrated bed pressure through the  $k$ th cell edge expressed in the local framework (Murillo and Navas-Montilla, 2016).

Using (23), the homogeneous integrated Eq. (20) can be augmented with the edge-split momentum contributions of the bed-pressure term as

$$\frac{d}{dt} \int_{\Omega_i} U \, d\Omega + \sum_{k=1}^{NE} \mathbf{R}_k^{-1} F(\hat{U})_k l_k = \sum_{k=1}^{NE} \mathbf{R}_k^{-1} H(\hat{U})_k l_k \quad (24)$$

and, including also the basal resistance term  $S_t$ , the complete integrated system can be expressed as



$$\frac{d}{dt} \int_{\Omega_i} \mathbf{U} d\Omega = - \sum_{k=1}^{NE} \mathbf{R}_k^{-1} (\mathbf{F}(\widehat{\mathbf{U}})_k - \mathbf{H}(\widehat{\mathbf{U}})_k) l_k + \int_{\Omega_i} \mathbf{S}_\tau(\mathbf{U}) d\Omega \quad (25)$$

Assuming a piecewise uniform representation of the conserved variables  $\mathbf{U}$  at the  $i$  cell for the time  $t = t^n$

$$\mathbf{U}_i^n = \frac{1}{A_i} \int_{\Omega_i} \mathbf{U}(x, y, t^n) d\Omega \quad (26)$$

where  $A_i$  is the discrete cell area, and using first-order explicit temporal integration, the value of the variables  $\mathbf{U}$  at the cells can be updated as

$$\mathbf{U}_i^{n+1} = \mathbf{U}_i^n - \frac{\Delta t}{A_i} \sum_{k=1}^{NE} \mathbf{R}_k^{-1} \mathbf{F}_k^l l_k + \frac{\Delta t}{A_i} \int_{\Omega_i} \mathbf{S}_\tau(\mathbf{U}) d\Omega \quad (27)$$

being  $\Delta t = t^{n+1} - t^n$  the time step and  $\mathbf{F}_k^l$  the explicit frictionless normal flux vector at the  $k$ th cell edge, including the conservative fluxes and the bed-pressure momentum contribution.

In this work, this frictionless flux vector is upwind computed using the approximate Riemann problem (RP) theory and a first-order Roe's solver for compressible shallow flows. Details on the flux computation have been extensively reported in Martínez-Aranda et al. (2021), Martínez-Aranda et al. (2020), Martínez-Aranda (2021) but, for the sake of completeness, a summary is included in Appendix B. The frictionless flux vector  $\mathbf{F}_k^l$  at the  $k$ th cell edge, separating the left  $i$  cell and the right  $j$  cell, is computed as

$$\mathbf{F}_k^l = \mathbf{F}(\widehat{\mathbf{U}}_i^n) + \sum_{m-} [(\tilde{\lambda}_m \tilde{\alpha}_m - \tilde{\beta}_m) \tilde{\mathbf{e}}_m]_k^n \quad (28)$$

where  $\tilde{\lambda}_{m,k}$  are the wave celerities at the edge, i.e. the eigenvalues of the Jacobian matrix of the RP,  $(\tilde{\mathbf{e}}_m)_k$  are the eigenvectors of the RP,  $\tilde{\alpha}_{m,k}$  denotes the wave strengths accounting for the discontinuity on the conservative variables and  $\tilde{\beta}_{m,k}$  are the source strengths which include the integrated bed pressure contribution through the cell edge. The subscript  $m-$  under the sums indicate that only the waves travelling inward the  $i$  cell are considered, leading to the upwind computation of the flux at the edge.

The numerical resolution the resistance cell-centered integral  $\int_{\Omega_i} \mathbf{S}_\tau(\mathbf{U}) d\Omega$  in (27) is open to different possibilities. First, considering the time-dependence, explicit and implicit resolution procedures can be distinguished. Second, the rotational invariance of the integrated resistance force is not straightforward in the 2D framework. The resolution procedure must guarantee that the net integrated resistance force does not depend on the discrete cell geometry. In this work, we propose and compare new efficient strategies for the explicit upwind and the implicit centered computation of the basal resistance term in non-Newtonian 2D shallow models.

#### 4. Explicit upwind computation of generalized basal resistance terms

In this work, two different novel strategies for the spatial discretization of the basal resistance source term are proposed. Both allow the explicit computation of the resistance cell-centered integral in (27) as

$$\int_{\Omega_i} \mathbf{S}_\tau(\mathbf{U}(x, y, t^n)) d\Omega = \sum_{k=1}^{NE} \mathbf{R}_k^{-1} \mathbf{T}(\widehat{\mathbf{U}}_i^n)_k l_k \quad (29)$$

where  $\mathbf{T}(\widehat{\mathbf{U}}_i^n)_k$  is the split contribution of the integrated basal resistance to the momentum at the  $k$ th cell edge.

Therefore, assuming a piecewise uniform representation of the conservative variables at the cells for the time  $t^n$ , the discrete contribution of the integrated basal resistance at the  $k$ th edge separating the left  $i$  cell from the right  $j$  cell,  $\mathbf{T}(\widehat{\mathbf{U}}_i^n, \widehat{\mathbf{U}}_j^n)_k$ , can be expressed in the local

eigenvector basis using the resistance strengths  $\tilde{\sigma}_{m,k}$  as

$$\mathbf{T}(\widehat{\mathbf{U}}_i^n, \widehat{\mathbf{U}}_j^n)_k = \sum_{m=1}^4 (\tilde{\sigma}_m \tilde{\mathbf{e}}_m)_k^n \quad (30)$$

and it can be added to the frictionless flux (28), leading to an augmented upwind flux  $\mathbf{F}_k^{l-}$  at the  $k$ th cell edge written as

$$\mathbf{F}_k^{l-} = \mathbf{F}_k^l - \sum_{m-} (\tilde{\sigma}_m \tilde{\mathbf{e}}_m)_k^n = \mathbf{F}(\widehat{\mathbf{U}}_i^n) + \sum_{m-} [(\tilde{\lambda}_m \tilde{\alpha}_m - \tilde{\beta}_m) \tilde{\mathbf{e}}_m]_k^n \quad (31)$$

This leads to a numerical flux formulation which also accounts for the basal resistance term and allows to write the final updating formula for the conservative variables as

$$\mathbf{U}_i^{n+1} = \mathbf{U}_i^n - \frac{\Delta t}{A_i} \sum_{k=1}^{NE} \mathbf{R}_k^{-1} \mathcal{F}_k^{l-} l_k \quad (32)$$

The definition of the edge-contribution of the integrated resistance  $\mathbf{T}(\widehat{\mathbf{U}}_i^n, \widehat{\mathbf{U}}_j^n)_k$  is the key point to ensure the correct computation of the two-dimensional basal resistance term.

#### 4.1. Classical normal-integrated approach

This procedure for computing the explicit edge-contribution was initially derived by Murillo and García-Navarro (2010) for pure turbulent Newtonian 2D flows, based on the friction term treatment proposed by Burguete et al. (2008) for the one-dimensional shallow water system. Then, this upwind normal approach was directly adapted for non-Newtonian 2D shallow flows (Murillo and García-Navarro, 2012) and widely used for dry granular and saturated mud/debris flows (Juez and Murillo, 2013; Juez et al., 2014; Martínez-Aranda et al., 2020, 2021).

The explicit centered integral of the basal resistance at the  $i$  cell is approximated as

$$\int_{\Omega_i} \mathbf{S}_\tau(\mathbf{U}) d\Omega \approx \sum_{k=1}^{NE} \left( \int_{\hat{x}} \mathbf{S}_{\text{nt}} d\hat{x} \right)_k l_k \quad (33)$$

where  $\mathbf{S}_{\text{nt}}$  is the basal resistance vector along the normal direction  $\hat{x}$  to the  $k$ th cell edge. The integrated basal resistance contribution through the edge is hence expressed in the global  $\mathbf{X} = (x, y)$  reference system as

$$(\tilde{\mathbf{S}}_{\text{nt}})_k \equiv \left( \int_{\hat{x}} \mathbf{S}_{\text{nt}} d\hat{x} \right)_k = \begin{pmatrix} 0 \\ -\frac{\tau_b(\mathbf{u} \cdot \mathbf{n})}{\rho_w} d_n n_x \\ -\frac{\tau_b(\mathbf{u} \cdot \mathbf{n})}{\rho_w} d_n n_y \\ 0 \end{pmatrix}_k \quad (34)$$

being  $d_{n,k}$  the integration distance along the normal to the cell edge (see Fig. 5).

Therefore, replacing (34) into (33) leads to

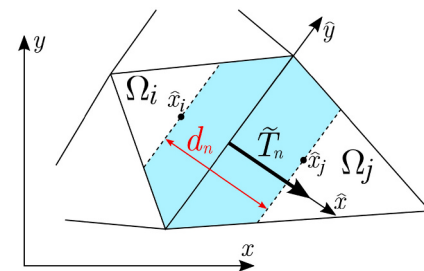


Fig. 5. Normal-integrated procedure for the integration of the 2D resistance force.

$$\int_{\Omega_i} S_\tau(U) d\Omega \approx \sum_{k=1}^{NE} R_k^{-1} R_k (\tilde{S}_{n\tau})_k l_k = \sum_{k=1}^{NE} R_k^{-1} T(\hat{U})_k l_k \quad (35)$$

with  $T(\hat{U})_k = R_k (\tilde{S}_{n\tau})_k$ . Therefore, the discrete edge-contribution of the basal resistance  $T(\hat{U}_i^n, \hat{U}_j^n)_k$  using the classical normal approach is computed as

$$T(\hat{U}_i^n, \hat{U}_j^n)_k = \begin{pmatrix} 0 \\ -\text{sgn}(\tilde{u}_n) \frac{|\tau_b(\tilde{u}_n)|}{\rho_w} d_n \\ 0 \\ 0 \end{pmatrix}_k \quad (36)$$

where  $d_n$  is the normal distance between the neighbouring cell centers and  $\tau_b(\tilde{u}_n)$  is the basal resistance computed using the edge-averaged normal flow velocity.

#### 4.2. Integral approach for the edge-integrated resistance force

In the integral approach, the cell-centered integral of the basal resistance in (29) is divided in contributions associated to the cell edges as

$$\int_{\Omega_i} S_\tau(U) d\Omega = \sum_{k=1}^{NE} R_k^{-1} \int_{\Omega_{k,i}} R_k S_\tau(U) d\Omega \quad (37)$$

where  $\Omega_{k,i}$  is the portion of the  $i$  cell associated to the  $k$ th cell edge, satisfying  $\sum_{k=1}^{NE} \Omega_{k,i} = \Omega_i$ . This associated portion corresponds to the discrete triangular area  $\Omega_{k,i} = 1/2 d_{n,i} l_k$ , being  $d_{n,i}$  the normal distance from the center of the  $i$  cell to the edge (Fig. 6). Therefore, assuming a piecewise representation of the conserved variables at the cells, the integral of the basal resistance associated to each edge can be simplified as

$$\int_{\Omega_{k,i}} R_k S_\tau(U) d\Omega = R_k S_\tau(U) \frac{1}{2} d_{n,i} l_k \quad (38)$$

The piecewise basal resistance vector projected into the local framework can be rewritten as

$$R_k S_\tau(U) = S_\tau(\hat{U}) = \begin{pmatrix} 0 \\ -\frac{\tau_b}{\rho_w} \mathbf{n}_u \cdot \mathbf{n} \\ -\frac{\tau_b}{\rho_w} \mathbf{n}_u \cdot \mathbf{t} \\ 0 \\ 0 \end{pmatrix}_k \quad (39)$$

where  $\mathbf{n}$  and  $\mathbf{t}$  are the normal and tangential unit vectors to the  $k$ th cell edge respectively. Replacing (38) and (39) into (37) leads to

$$\int_{\Omega_i} S_\tau(U) d\Omega = \sum_{k=1}^{NE} R_k^{-1} S_\tau(\hat{U}) \frac{1}{2} d_{n,i} l_k = \sum_{k=1}^{NE} R_k^{-1} T(\hat{U})_k l_k \quad (40)$$

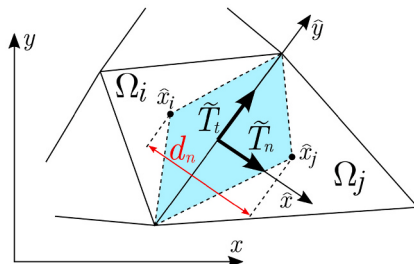


Fig. 6. Integral procedure for the integration of the 2D resistance force.

with  $T(\hat{U})_k = S_\tau(\hat{U}) \frac{1}{2} d_{n,i}$ . Physically, the basal resistance term should always act slowing down the flow. In the extreme case, the non-Newtonian resistance contribution must stop the flow completely, maintaining the quiescent equilibrium when the component of the gravitational force tangential to the bed surface remains below the frictional/cohesive yield strength. Therefore, it is important to stress that the discrete edge-contribution of the basal resistance,  $T(\hat{U}_i^n, \hat{U}_j^n)_k$ , should be opposite to the frictionless discharge at the cell edge and is hence defined as

$$T(\hat{U}_i^n, \hat{U}_j^n)_k = \begin{pmatrix} 0 \\ \tilde{T}_n \\ \tilde{T}_t \\ 0 \end{pmatrix}_k = \begin{pmatrix} 0 \\ -\text{sgn}(m_n) \frac{\tilde{\tau}_b}{\rho_w} \frac{|\tilde{u}_n|}{\sqrt{\tilde{u}_n^2 + \tilde{v}_t^2}} \frac{1}{2} d_n \\ -\text{sgn}(m_t) \frac{\tilde{\tau}_b}{\rho_w} \frac{|\tilde{v}_t|}{\sqrt{\tilde{u}_n^2 + \tilde{v}_t^2}} \frac{1}{2} d_n \\ 0 \end{pmatrix}_k \quad (41)$$

where  $(\tilde{T}_n)_k$  and  $(\tilde{T}_t)_k$  represent the discrete edge-contribution of the integrated basal resistance along the normal and tangential directions to the  $k$ th cell edge,  $(d_n)_k = d_{n,i} + d_{n,j}$  is the distance between the cell center along the normal direction to the edge and  $(\tilde{\tau}_b)_k = \frac{1}{2}(\tau_{b,i} + \tau_{b,j})$  is the averaged bed shear stress at the  $k$ th cell edge, being  $\tau_{b,i}$  and  $\tau_{b,j}$  the corresponding resistance value at the neighbouring cells. Note that  $(m_n, m_t)_k$  in (41) denote the normal and tangential frictionless mass rates at the  $k$ th cell edge, respectively, which are computed using the properties of the approximate RP eigenstructure as in (87).

#### 4.3. Differential approach for the edge-integrated resistance force

The differential strategy is based on treating the resistance source term as a non-conservative momentum flux across the cell boundary. Assuming a basal resistance flux matrix  $\mathbf{Q}(U, D)$ , depending on both the conserved variables  $U$  and the integration-distance vector  $D = (0, \Delta x, \Delta y, 0)^T$ , which satisfies the condition

$$S_\tau(U) = \nabla \cdot \mathbf{Q}(U, D) \quad (42)$$

allows to use the Gauss theorem to express the basal resistance contribution at the cell as

$$\int_{\Omega_i} S_\tau(U) d\Omega = \int_{\Omega_i} \nabla \cdot \mathbf{Q}(U, D) d\Omega = \oint_{\partial\Omega_i} \mathbf{Q}(U, D) \cdot \mathbf{n} dl \quad (43)$$

Therefore, a valid expression for the resistance flux matrix  $\mathbf{Q}(U, D)$  is

$$\mathbf{Q}(U, D) = \begin{pmatrix} Q_x(U, D) & Q_y(U, D) \end{pmatrix} = \begin{pmatrix} 0 & 0 \\ -\frac{\tau_b}{\rho_w} \mathbf{n}_u \cdot \mathbf{d}_c & 0 \\ 0 & -\frac{\tau_b}{\rho_w} \mathbf{n}_u \cdot \mathbf{d}_c \\ 0 & 0 \end{pmatrix} \quad (44)$$

with  $\mathbf{n}_u = (n_{ux}, n_{uy})$  and  $\mathbf{d}_c = (\Delta x, \Delta y)$  (Fig. 7).

Furthermore, the resistance flux matrix (44) is invariant under rotation since it satisfies

$$\nabla \cdot \mathbf{Q}(U, D) = R_k^{-1} \hat{\nabla} \cdot \mathbf{Q}(R_k U, R_k D) \quad (45)$$

allowing to express

$$\mathbf{Q}(U, D) \cdot \mathbf{n} = R_k^{-1} Q_x(R_k U, R_k D) \quad (46)$$

It is worth noting that, in this case,  $Q_x(R_k U, R_k D) \equiv Q_x(\hat{U}, \hat{D}) =$

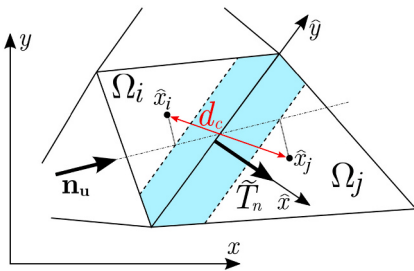


Fig. 7. Differential procedure for the integration of the 2D resistance force.

$Q_x(U, D)$  due to the rotation invariance of the scalar product  $\mathbf{n}_u \cdot \mathbf{d}_c = (\mathbf{R}_k \mathbf{n}_u) \cdot (\mathbf{R}_k \mathbf{d}_c)$  (Godlewski and Raviart, 1996b).

Replacing (46) into (43) leads to the expression

$$\int_{\Omega_i} S_\tau(U) d\Omega = \sum_{k=1}^{NE} R_k^{-1} Q_x(\hat{U}, \hat{D})_k l_k = \sum_{k=1}^{NE} R_k^{-1} T(\hat{U})_k l_k \quad (47)$$

with  $T(\hat{U})_k = Q_x(\hat{U}, \hat{D})_k$ . As in the case of the integral strategy, the basal resistance term should always act slowing down the flow and hence the discrete edge-contribution,  $T(\hat{U}_i^n, \hat{U}_j^n)$ , should be opposite to the frictionless mass rate at the cell edge, leading to

$$T(\hat{U}_i^n, \hat{U}_j^n)_k = \begin{pmatrix} 0 \\ \tilde{T}_n \\ 0 \\ 0 \end{pmatrix}_k = \begin{pmatrix} 0 \\ -\text{sgn}(m_n) \frac{\tilde{\tau}_b}{\rho_w} |\tilde{n}_{ux} \Delta x + \tilde{n}_{uy} \Delta y| \\ 0 \\ 0 \end{pmatrix}_k \quad (48)$$

where  $(\tilde{T}_n)_k$  represents the discrete edge-contribution of the integrated basal resistance along the normal direction,  $(\tilde{\tau}_b)_k = \frac{1}{2}(\tau_{bi} + \tau_{bj})$  is the edge-averaged bed shear stress,  $(\tilde{n}_{ux}, \tilde{n}_{uy})_k$  are the components of the unit vector of the edge-averaged flow direction and  $\text{sgn}(m_n)_k$  denotes the direction of the frictionless mass rate at the time  $t = t^n$  along the normal direction to the  $k$ th cell edge, computed as in (87).

It is worth mentioning that, using the differential approach leads to an estimation of the resistance force disconnected from the edge orientation but only depending on the flow direction and the distance between cell centers. Therefore, this procedure liberates the basal resistance force exerted against the flow from the mesh topology.

## 5. Implicit centered computation for quadratic basal resistance terms

If an implicit centered strategy is considered for the basal resistance term, the resistance integral in (27) is expressed as a function of the piecewise conservative variables at the time  $t = t^{n+1}$  for each  $i$  cell as

$$\int_{\Omega_i} S_\tau(U(x, y, t^{n+1})) d\Omega = A_i S_\tau(U_i^{n+1}) \quad (49)$$

and the final updating formula can be expressed as

$$U_i^{n+1} = U_i^n - \frac{\Delta t}{A_i} \sum_{k=1}^{NE} R_k^{-1} F_k^{\downarrow-} l_k + \Delta t S_\tau(U_i^{n+1}) \quad (50)$$

being  $F_k^{\downarrow-} = (F_1, F_2, F_3, F_4)^{\downarrow-}$  the frictionless upwind flux vector (28) at the cell  $k$ th edge and  $S_\tau(U_i^{n+1})$  the implicit cell-centered basal resistance contribution at the  $i$  cell, computed as

$$S_\tau(U_i^{n+1}) = \begin{pmatrix} 0 \\ -(\tau_b n_{ux})_i^{n+1} / \rho_w \\ -(\tau_b n_{uy})_i^{n+1} / \rho_w \\ 0 \end{pmatrix} \quad (51)$$

Based on the development of Xia and Liang (2018) for the implicit computation of turbulent flows, we derive here a novel approach for the cell-centered integration of the resistance term. If the frictional non-linear viscoplastic model (7) with behaviour exponent  $m = 2$  is considered, the basal resistance  $\tau_b$  can be expressed as

$$\tau_b = \tau_b n_u = \tau_f \frac{rh_u}{|rh_u|} + \frac{25}{4} \mu_p \frac{|rh_u| rh_u}{(rh)^2 h^2} \quad (52)$$

where  $rh_u$  is the normalized mass rate in the global horizontal coordinate system  $\mathbf{X} = (x, y)$ , and hence the conservative variables are updated using (50) as

$$(rh)_i^{n+1} = (rh)_i^n - \frac{\Delta t}{A_i} \sum_{k=1}^{NE} (F_1)_k^{\downarrow-} l_k \quad (53a)$$

$$(rh_u)_i^{n+1} = (m_x)_i^{n+1} - \Delta t \left( \frac{\tau_f}{\rho_w} \frac{rh_u}{|rh_u|} + \frac{25}{4} \frac{\mu_p}{\rho_w} \frac{|rh_u| rh_u}{(rh)^2 h^2} \right)_i^{n+1} \quad (53b)$$

$$(rhv)_i^{n+1} = (m_y)_i^{n+1} - \Delta t \left( \frac{\tau_f}{\rho_w} \frac{rhv}{|rhv|} + \frac{25}{4} \frac{\mu_p}{\rho_w} \frac{|rhv| rhv}{(rh)^2 h^2} \right)_i^{n+1} \quad (53c)$$

$$(h\phi^\chi)_i^{n+1} = (h\phi^\chi)_i^n - \frac{\Delta t}{A_i} \sum_{k=1}^{NE} (F_4)_k^{\downarrow-} l_k \quad (53d)$$

where  $h_i^{n+1} = (rh)_i^{n+1} - (h\phi^\chi)_i^{n+1}$  is the updated flow depth,  $(m_x, m_y)_i^{n+1}$  are the cell-centered frictionless mass rate along the  $x$ - and  $y$ -coordinates respectively updated at the time  $t^{n+1}$ , computed as

$$(m_x)_i^{n+1} = (rh_u)_i^n - \frac{\Delta t}{A_i} \sum_{k=1}^{NE} (F_2 n_x - F_3 n_y)_k^{\downarrow-} l_k \quad (54)$$

$$(m_y)_i^{n+1} = (rhv)_i^n - \frac{\Delta t}{A_i} \sum_{k=1}^{NE} (F_2 n_y + F_3 n_x)_k^{\downarrow-} l_k$$

and  $\tau_{f,i}^{n+1}$  denotes the updated frictional yield strength as

$$\tau_{f,i}^{n+1} = (\rho_i^{n+1} - \rho_w) g h_i^{n+1} \tan \delta_f \quad (55)$$

being  $\rho_i^{n+1} = \rho_w (rh)_i^{n+1} / h_i^{n+1}$  the updated bulk density.

Note that updated conservative variables  $(rh)_i^{n+1}$ ,  $(h\phi^\chi)_i^{n+1}$ ,  $(m_x)_i^{n+1}$  and  $(m_y)_i^{n+1}$  can be computed from the conservative variables at the current time  $t^n$  despite the value of the normalized mass rate updated at the time  $t^{n+1}$  remains unknown.

Manipulating (53b) and (53c), a solution for the updated cell-centered value of the mass rate along the  $x$ - and  $y$ -coordinates in the  $i$  cell,  $(rh_u)_i^{n+1}$  and  $(rhv)_i^{n+1}$  respectively, can be derived as

$$(rh_u)_i^{n+1} = \mathcal{T}_i (m_x)_i^{n+1} \quad (56)$$

being  $\mathcal{T}_i$  the implicit basal resistance factor for correcting the frictionless mass rate, defined (see Appendix C) as

$$\mathcal{T}_i = \frac{-1 + \sqrt{1 + 25\Delta t \frac{\mu_p}{\rho_w} (rh)^{-2} h^{-2} \left( \sqrt{\mathcal{M}_x^2 + \mathcal{M}_y^2} - \Delta t \frac{\tau_f}{\rho_w} \right)}}{\frac{25}{2} \Delta t \frac{\mu_p}{\rho_w} (rh)^{-2} h^{-2} \sqrt{\mathcal{M}_x^2 + \mathcal{M}_y^2}} \quad (57)$$

where, for the sake of clarity,  $\text{rh} \equiv (\text{rh})_i^{n+1}$ ,  $h \equiv h_i^{n+1}$ ,  $\mathcal{M}_x \equiv |m_x|_i^{n+1}$ ,  $\mathcal{M}_y \equiv |m_y|_i^{n+1}$  and  $\tau_f \equiv (\tau_f)_i^{n+1}$  are known variables at the time  $t^{n+1}$ .

It is worth mentioning that, in order that the basal resistance term does not change the frictionless flow direction neither accelerate the flow, the implicit basal resistance factor must satisfy  $\mathcal{T}_i \in [0, 1]$ . The expression (57) only ensures non-negativity if

$$\tau_f \leq \frac{\rho_w}{\Delta t} \sqrt{\mathcal{M}_x^2 + \mathcal{M}_y^2} \quad (58)$$

is guaranteed and hence  $\tau_f > \rho_w \sqrt{\mathcal{M}_x^2 + \mathcal{M}_y^2} / \Delta t$ . When the yield stress contribution is larger than the frictionless momentum, the updated mass rate  $(\text{rhu}, \text{rvh})_i^{n+1}$  would be null.

## 6. Numerical tests

This section is structured as follows: [case 6.1](#) compares the three explicit upwind approaches for a one-directional dambreak of a Bingham fluid a 1D single-row square mesh ([6.1.A](#)) and 2D meshes ([6.1.B](#)); [case 6.2](#) studies the two-dimensional spreading of a cylindrical volume using the three explicit upwind approaches in different 2D mesh topologies, considering the frictional Herschel-Bulkley ([6.2.A](#)) and the Bingham ([6.2.B](#)) closure models for the basal shear stress; [case 6.3](#) analyzes the performance of the implicit centered approach and the three explicit upwind strategies for simulating steady flows of a Herschel-Bulkley fluid in both 1D single-row square mesh ([6.3.A](#)) and 2D meshes ([6.3.B](#)); [case 6.4](#) is devoted to compare the implicit centered and the differential explicit upwind approaches for a circular dambreak of a frictional Herschel-Bulkley fluid, in terms of mesh convergence, accuracy and performance; and, finally, [case 6.5](#) demonstrates the stability and consistency of the implicit centered and the proposed explicit upwind strategies when dealing with realistic unsteady dambreak flows of debris materials.

### 6.1. Explicit upwind resistance: one-directional dambreak of a Bingham fluid

The aim of this synthetic test is to analyze the behavior of the novel integral and differential procedures for the explicit upwind discretization of the basal resistance term. [Hung \(1995\)](#) used the theory of roll waves in plastic medium to derive an analytical 1D solution for the runout distance of a plastic-type dambreak assuming null inertial forces, constant work of the shear stress and parabolic free surface after the detention of the flow. Considering an initial 30.5 m high and 305 m long dambreak over fixed flat bed of a plastic fluid with constant  $\rho = 1835 \text{ kg/m}^3$  density and  $c = 2390 \text{ Pa}$  shear strength, the runout distance reached by the wave front is  $x = 1896 \text{ m}$ . [Naef et al. \(2006\)](#) took this solution as benchmark test for their one-dimensional model and approximated the plastic resistance using a Bingham model with a yield strength  $\tau_y = 1500 \text{ Pa}$  and a plastic viscosity  $\mu_B = 100 \text{ Pa}\cdot\text{s}$ , obtaining a runout distance of  $x \approx 1850 \text{ m}$ .

#### Case 6.1.A: 1D framework dambreak

For a pure one-dimensional RP, the novel integral and differential approaches for the basal resistance discretization should exactly converge to the same solution since the integrated resistance contributions reduce to

$$\text{Integral approach : } \left\{ \begin{array}{l} |(\tilde{T}_n)_k| = \frac{\tilde{\tau}_b}{\rho_w} \Delta x \\ |(\tilde{T}_t)_k| = 0 \end{array} \right.$$

$$\text{Differential approach : } |(\tilde{T}_n)_k| = \frac{\tilde{\tau}_b}{\rho_w} \Delta x$$

A 1D mesh of square cells is considered with  $\Delta x = 1 \text{ m}$  and  $\text{CFL}=1$ .

The cohesive Bingham resistance model (6) is set with  $\rho = 1835 \text{ kg/m}^3$ ,  $\mu_B = 100 \text{ Pa}\cdot\text{s}$  and  $\tau_y = 1500 \text{ Pa}$ . The temporal evolution of the free surface and velocity with the integral and the differential resistance integration strategies are shown in [Fig. 8](#).

First, the solution obtained with both strategies is exactly the same and, second, both approaches are able to completely stop the flow with a final runout distance  $x = 1885 \text{ m}$ . This demonstrates that both strategies offer good approximations of the integrated basal resistance force acting against the flow and are able to predict the stop-going mechanism in non-Newtonian flows.

#### Case 6.1.B: 2D framework dambreak

In order to analyze the dependence of the integral and differential resistance discretization on the mesh topology in 2D frameworks, this one-directional benchmark test is simulated assuming a 10 m wide and 2500 m long channel discretized using a 25,000 cells orthogonal mesh, a 50,000 cells triangle-structured mesh and a 50,361 cells triangle-unstructured mesh ([Fig. 9](#)). The averaged edge length is  $l_k \approx 1 \text{ m}$  for the three meshes, in order to use comparable mesh refinements. The CFL is 0.5 for the orthogonal mesh and 1.0 for the triangular meshes.

The results obtained with novel integral and differential approaches are compared with the method classical proposed by [Murillo and García-Navarro \(2012\)](#). The final free surface after the detention of the one-directional dambreak wave is plotted in [Figs. 10, 11](#) and [12](#). The normal-integrated discretization dealing with non-Newtonian shear stresses involves a high mesh dependence, since the quantity of resistance force applied against the flow is directly influenced by edge orientation respect to the flow direction. The resistance force converges to the 1D-framework value when orthogonal meshes oriented with the flow direction are used, but shows important variations in triangular meshes depending on the mesh topology ([Fig. 10](#)).

Conversely, the integral discretization of the basal resistance leads to mesh-independent results in the 2D framework ([Fig. 11](#)). However, differences appear respect to the pure 1D-framework results. These differences are directly related to the closed boundary edges at the channel lateral sides, since it is required that these edges also insert a proportional quantity of resistance force against the flow in order to converge to the pure 1D-framework solution. However, in these edges the local RP is not defined and hence the resolution requires the implementation of special boundary conditions, which is not the scope of this work.

Finally, the results with the differential approach for the discretization of the basal resistance contribution show fully mesh-independence in the 2D framework ([Fig. 12](#)) and also converge exactly to the solution obtained in the pure 1D-framework.

### 6.2. Explicit upwind resistance: 2D large-scale spreading of a cylindrical non-Newtonian volume

The spreading of a cylindrical volume is one of the most extended benchmarking test to analyze the behaviour of 2D numerical models for frictional flows ([Pirulli et al., 2007; Juez and Murillo, 2013](#)). Using different mesh types helps to point out numerical issues in the discretization of the homogeneous fluxes and source terms, since the spreading wave must maintain the circular shape regardless of the mesh topology and refinement. These discretization problems are further aggravated in large-scale and long-term simulations.

In order to analyze the performance of both the integral and the differential approaches for the discretization of the 2D basal resistance term, in comparison with the classical normal-integrated procedure ([Murillo and García-Navarro, 2012; Juez and Murillo, 2013; Martínez-Aranda et al., 2020](#)), a quiescent semicircular volume with initial height  $h_0 = 25 \text{ m}$  and radius  $R_0 = 100 \text{ m}$  of a non-Newtonian material is considered. The two-dimensional flat-bed spatial domain, with  $x = [-1200, 1200] \text{ m}$  and  $y = [0, 1200] \text{ m}$ , is discretized using the three different meshes (see [Fig. 9](#)) which have been summarized in [Table 1](#).

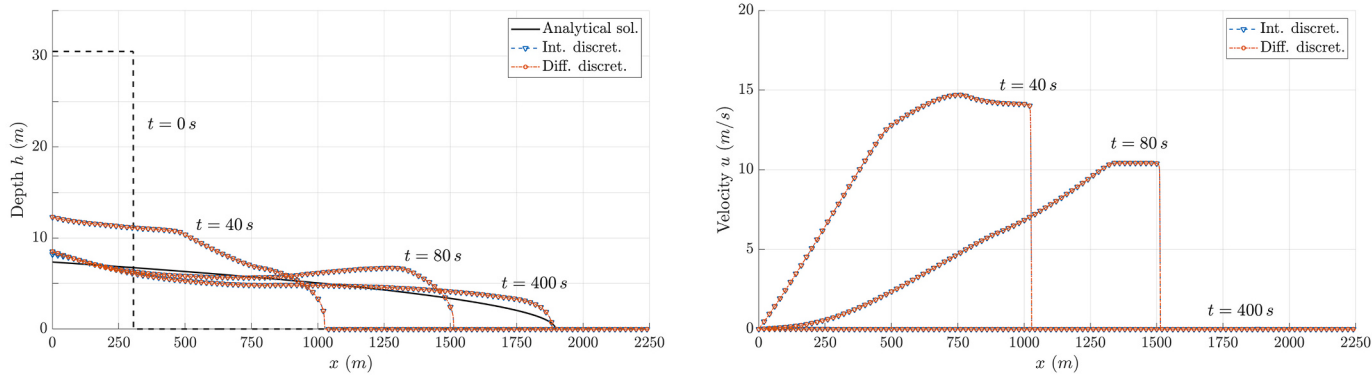


**Fig. 8.** Test 6.1.A – Temporal evolution of the flow depth and velocity for the Bingham dambreak using the explicit upwind integral and differential approaches in a 1D mesh.

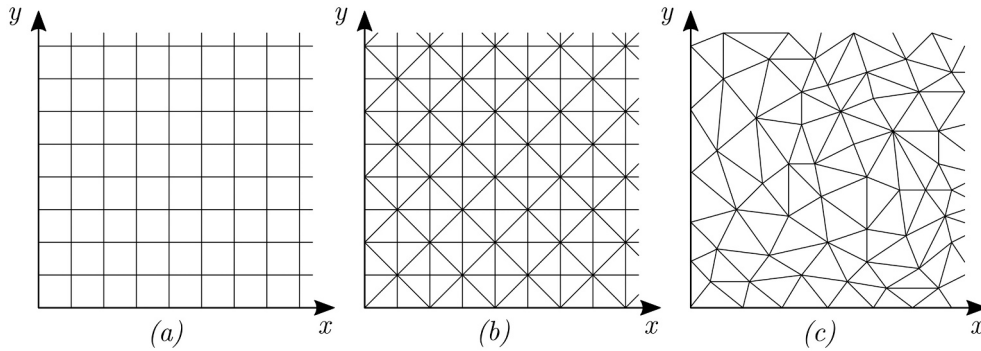


**Fig. 9.** Test 6.1.B – Topology of the 2D meshes: (a) orthogonal mesh, (b) triangle structured and (c) triangle unstructured.

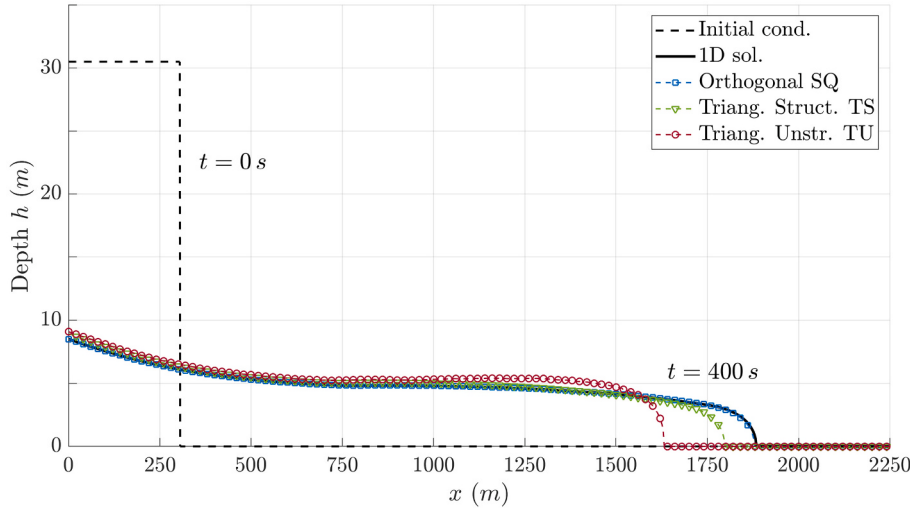


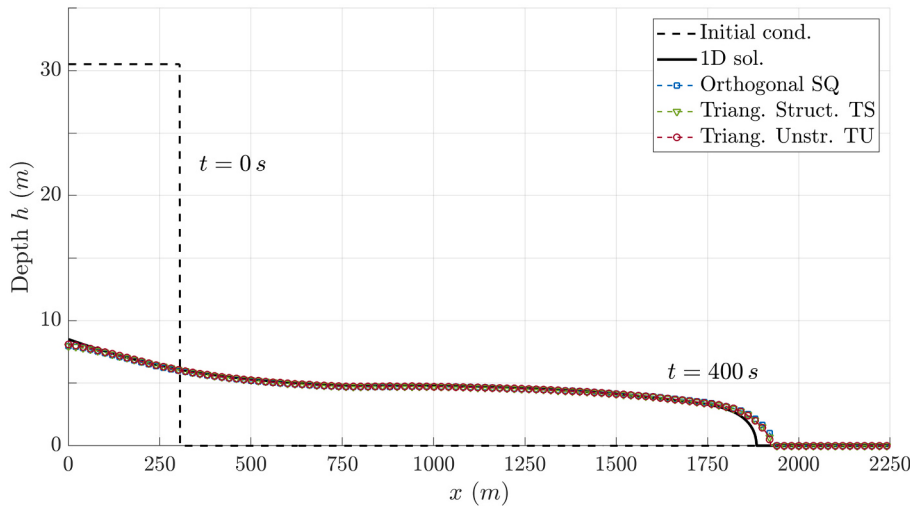
**Fig. 10.** Test 6.1.B – Final profile for the one-directional Bingham dambreak using the normal-integrated discretization of the basal resistance in different 2D meshes.

#### Case 6.2.A: frictional non-linear viscoplastic flow

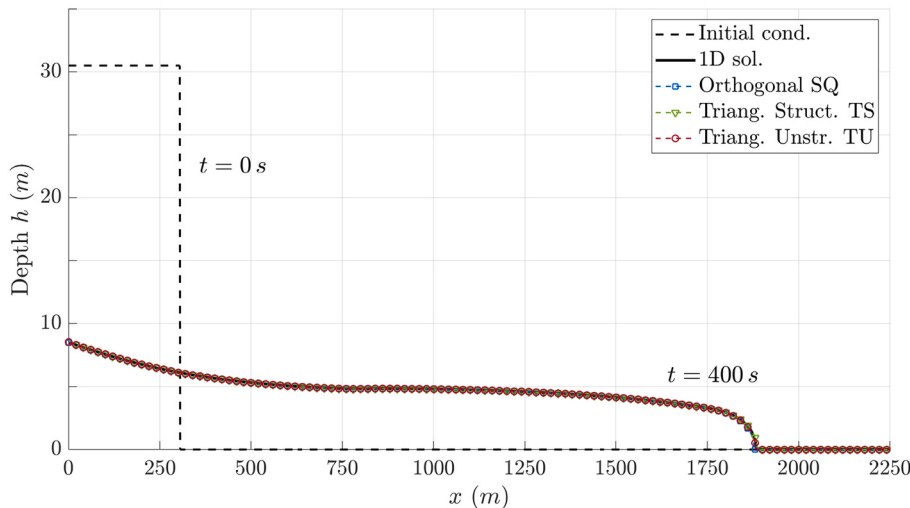
A uniform solid concentration  $\phi = 0.6$  is set at the initial time with solid density  $\rho_s = 2500 \text{ kg/m}^3$ , leading to a bulk density  $\rho = 1900 \text{ kg/m}^3$ . The basal shear stress is modelled using the frictional Herschel-Bulkley model (7), with behaviour exponent  $m = 2$ , plastic viscosity  $\mu_p = 5 \text{ Pa}\cdot\text{s}^2$  and basal stability angle  $\delta_f = 1^\circ$ . The CFL is set to 0.5 for the orthogonal (SQ) mesh and 1.0 for both triangular (TS and TU) meshes. The final simulation time is 150 s, enough to ensure that the spreading wave stops completely.

Fig. 13 shows the depth  $h$  with the orthogonal SQ mesh once the flow

totally stops. The dashed red line represents a perfect circle  $R = 1050 \text{ m}$ . The normal-integrated procedure (a) is highly mesh dependent and tends to align markedly with the mesh main-directions  $x = 0$  and  $y = 0$ . This behavior was previously reported by Pirulli et al. (2007) and Juez and Murillo (2013) but it was erroneously attributed to an insufficient mesh refinement, although further reducing the spatial discretization helps to slightly correct this undesirable effect in short-term and small-scale simulations (Pirulli et al., 2007). Nevertheless, this large-scale numerical experiment shows that the alignment of the flow with the mesh main-directions is directly related to the loss of the rotation



**Fig. 11.** Test 6.1.B – Final profile for the one-directional Bingham dambreak using the integral discretization of the basal resistance in different 2D meshes.



**Fig. 12.** Test 6.1.B – Final profile for the one-directional Bingham dambreak using the differential discretization of the basal resistance in different 2D meshes.

**Table 1**  
2D meshes considered for the spatial discretization in tests 6.2.A and 6.2.B.

Topology	Number of cells	Number of edges	Cell area	Edge length
Orthogonal (SQ)	115 200	231 120	25 m <sup>2</sup>	5 m
Triangle structured (TS)	230 400	346 320	12.5 m <sup>2</sup>	≈5 m
Triangle unstructured (TU)	230 555	346 498	≈12.5 m <sup>2</sup>	≈5 m

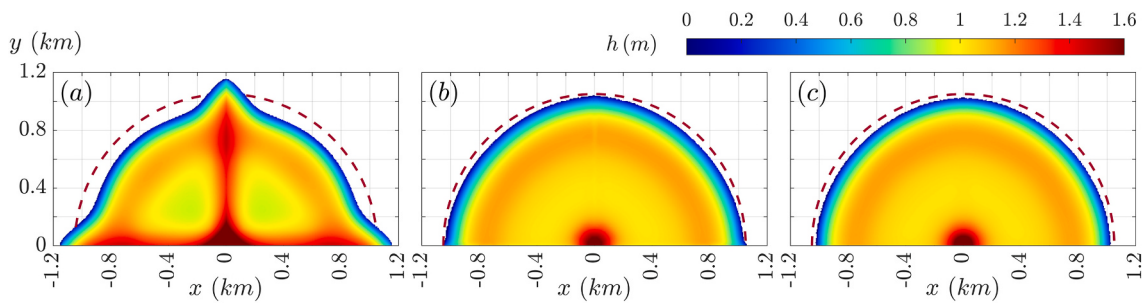
invariant property of the integrated basal resistance contribution. This loss of the invariance under rotation of the flow is caused by the erroneous procedure for including the 2D resistance term into the local plane RP at the cell edges.

Both the integral (b) and differential (c) approaches derived in this work maintain approximately the circular shape for the spreading wave until the flow detention, with a quite similar runout distance. However, the integral procedure shows slight alterations on the final flow depth aligned with the mesh main-directions. This small variation on the wave spreading shape can be directly related to the estimation of the tangential basal resistance along the main-directions  $x = 0$  and  $y = 0$ . It is worth mentioning that, during the first stages of the spreading

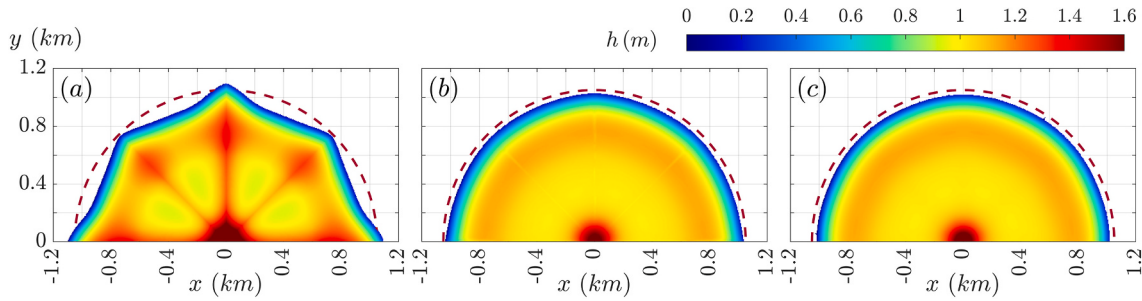
( $t < 25$  s), the normal-integrated procedure (a) is able to maintain approximately the circular wave shape but, as time progresses, the differences on the discretized resistance force depending on the mesh-flow alignment lead to an unphysical spreading shape at the final time.

Fig. 14 depicts the depth  $h$  distribution predicted with the triangle structured TS mesh after the flow totally stops. The dashed red line represents a perfect circle  $R = 1050$  m. Again the normal-integrated procedure (a) tends to align with the mesh main-directions ( $x = 0$ ,  $y = 0$  and  $|x| = |y|$ ) whereas both the integral (b) and differential (c) approaches maintain the circular shape for the spreading wave. Nevertheless, as with the orthogonal mesh, the integral procedure shows slight variations on the final flow depth aligned with the mesh main-directions.

Regarding the triangular unstructured TU mesh (Fig. 15), the three strategies for the integration of the basal resistance contribution are able to maintain the circular shape for the spreading wave since main-directions do not exist for this mesh topology. However, a marked roughness appears at the final free surface when the normal-integrated resistance strategy (a) is used. This free surface roughness with triangle unstructured meshes was also reported in Murillo and García-Navarro (2012) and Martínez-Aranda et al. (2020) and erroneously attributed to the depth data interpolation between cell center and nodes



**Fig. 13.** Test 6.2.A – Final depth  $h$  (m) with the orthogonal SQ mesh: (a) Normal-integrated, (b) Integral and (c) differential basal resistance contributions.



**Fig. 14.** Test 6.2.A – Final depth  $h$  (m) with the triangle structured TS mesh: (a) Normal-integrated, (b) Integral and (c) differential basal resistance contributions.

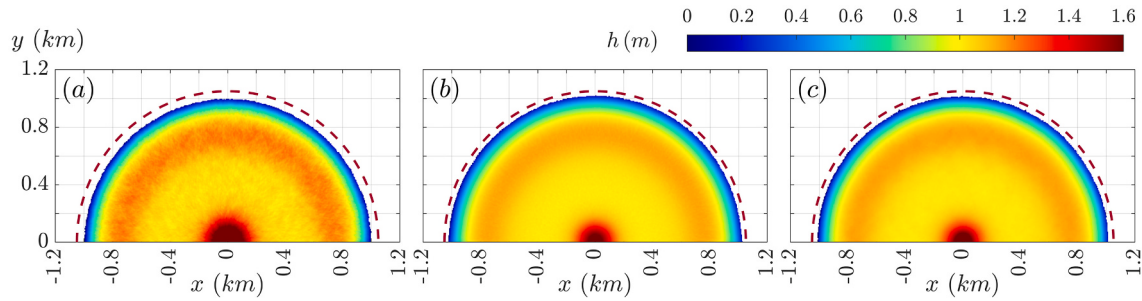


**Fig. 15.** Test 6.2.A – Final depth  $h$  (m) with the triangle unstructured TU mesh: (a) Normal-integrated, (b) Integral and (c) differential basal resistance contributions.

in Juez and Murillo (2013). Contrarily, the integral approach is able to avoid the free surface roughness and the differential strategy reduces these small-scale irregularities considerably, demonstrating that it is again an undesirable effect of the normal-integrated procedure for the integration of the 2D basal resistance vector.

The incorrect inclusion of the 2D basal resistance term into the local plane RP at the cell edges leads to highly mesh dependent results, since the quantity of integrated resistance force opposed to the flow movement is greatly affected by the edges orientation. Fig. 16 (left) depicts the temporal evolution of the wave-front location along the diagonal line  $x = y$  for the three explicit integration strategies considered, whereas Fig. 16 (right) shows the final depth along the same line. For the first stages of the spreading flow ( $t < 25$  s), the runout distance is quite similar with the three mesh topologies analysed, regardless of the basal resistance integration strategy. Only when the time-of-flow is large enough, thanks to the large-scale spatial domain of this numerical case, important deviations on the runout distance start to appear with the normal-integrated strategy (a) which depend on the mesh topology. These deviations are directly related to the orientation of the flow with the mesh main-directions and lead to different final depth profiles for each of the mesh topologies considered.

Contrarily, both the integral (b) and differential (c) strategies for the 2D basal resistance integration are able to maintain a runout distance

evolution similar for the three mesh topologies considered. Only at the final spreading flow stages, slight deviations appear between the orthogonal SQ mesh and the triangular TS and TU meshes and these deviations are probably more associated to the different cell area (see Table 1) than to the orientation of the flow with the respective mesh main-directions. Therefore, both new approaches offer quite similar results for final depth along the diagonal  $x = y$  line regardless of the mesh topology.

#### Case 6.2.B: cohesive Bingham flow

When a cohesive-type yield strength  $\tau_y$  is involved in the rheology (as in the Bingham formula (6)) and the classical normal-integrated procedure is used, the loss of the rotational invariance of the 2D integrated resistance force leads to even more marked flaws in the numerical solution. This occurs because the yield strength opposed to the material movement does not depend on the flow depth  $h$ , as happens with frictional-type stresses, but takes a constant shear stress value.

Fig. 17 shows the final depth  $h$  distribution for the spreading of a large-scale quiescent semicircular volume with initial height  $h_0 = 25$  m and radius  $R_0 = 100$  m of a cohesive Bingham fluid. The domain extension, mesh topology and simulation setup are the same as in the above case with a frictional-type material. The cohesive yield strength is 500 Pa and the dynamic viscosity of the material  $\mu_B = 8$  Pa·s, with a bulk

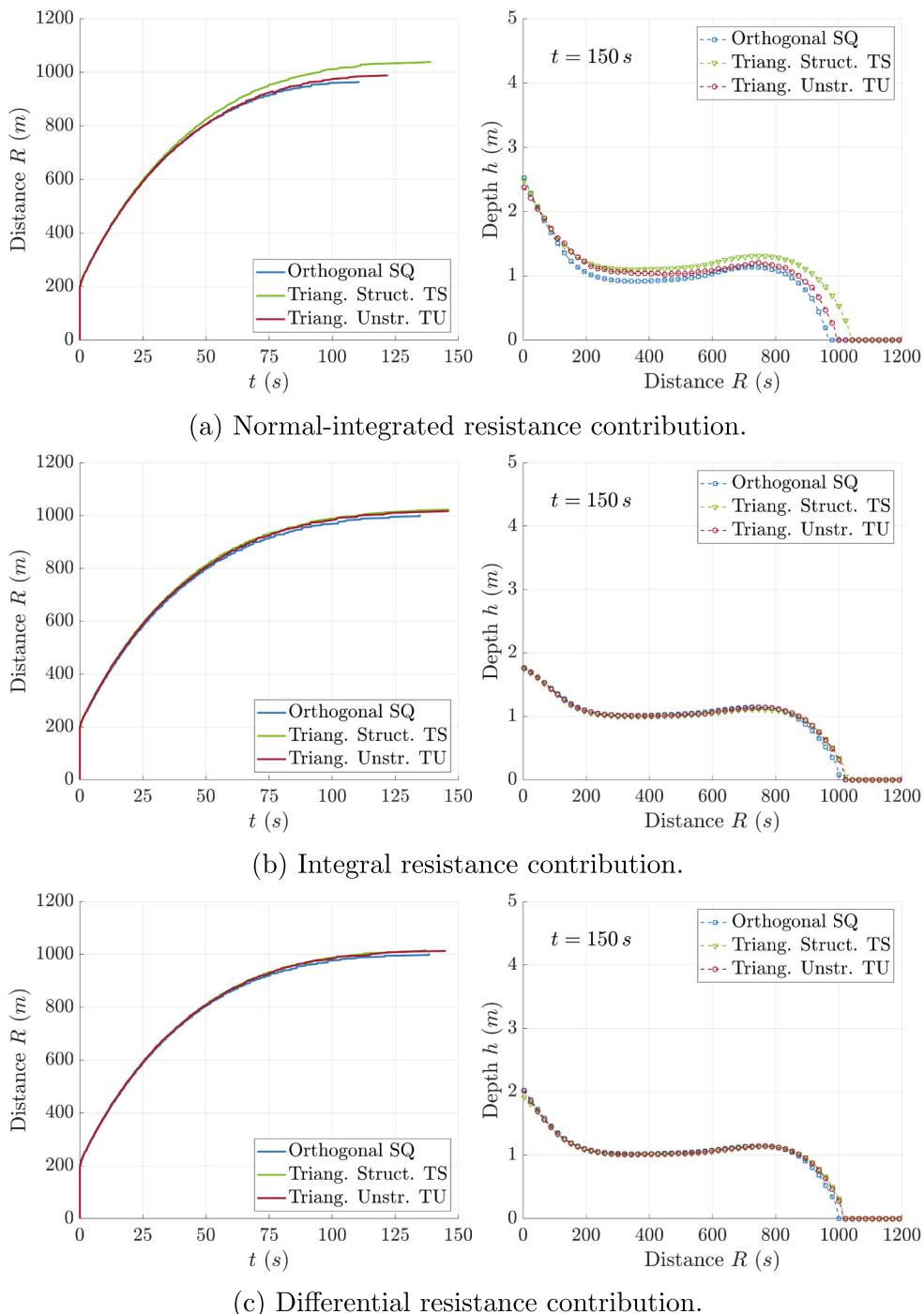


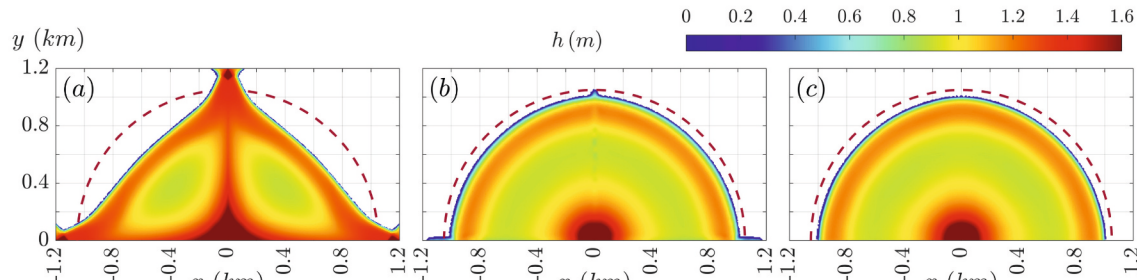
**Fig. 16.** Test 6.2.A – (left) Temporal evolution of the runout distance and (right) final depth along the diagonal line  $x = y$ . (a) Normal-integrated resistance contribution. (b) Integral resistance contribution. (c) Differential resistance contribution.

density  $\rho = 1900 \text{ kg/m}^3$ . Results for the orthogonal, triangle structured and triangle unstructured mesh topologies are shown with the three explicit upwind methods considered for the discretization of the 2D basal resistance contribution. The dashed red line represents a perfect circle  $R = 1050 \text{ m}$ .

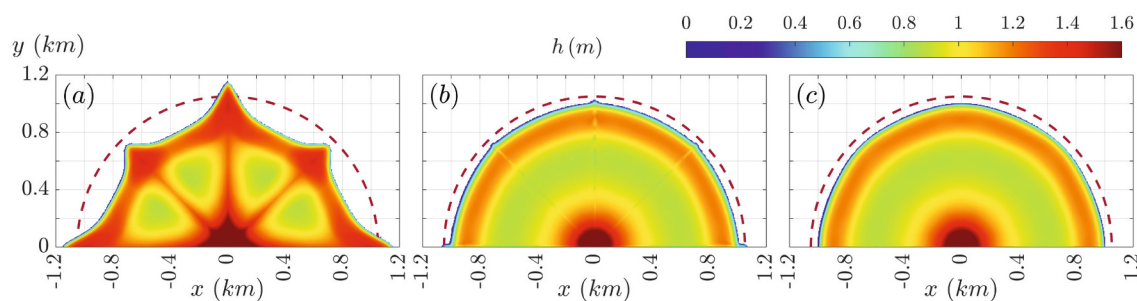
When using structured orthogonal and triangle meshes (see (i) and (ii) in Fig. 17), the loss of the invariance under rotation of the 2D integrated basal resistance force with the normal-integrated procedure (a) for the Bingham rheology is clear and even more marked than with the frictional dilatant relation. The integral approach (b) maintains reasonably well the circular shape but its flaws in cell edges perfectly

aligned with the flow direction are evident here, leading to slightly larger runout distance along the mesh main-direction. Nevertheless, the differential approach (c) maintains the well the semicircular shape of the wave spreading and only an indiscernible asymmetry is observed.

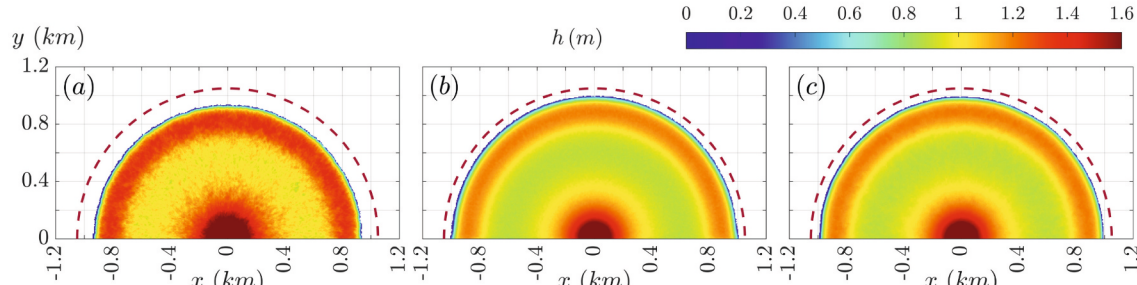
On the other hand, when using the triangular unstructured mesh (see (iii) in Fig. 17), the three strategies for the explicit upwind discretization of the 2D basal resistance contribution maintain the circular shape of the spreading wave. However, the normal-integrated procedure (a) shows a small final runout distance and a marked roughness in the final free surface as a consequence of the influence of the mesh direction on the integrated resistance force. Both the integral (b) and differential (c)



(i) Orthogonal mesh.



(ii) Triangle structured mesh.



(iii) Triangle unstructured mesh.

**Fig. 17.** Test 6.2.B – Final depth  $h$  (m) with the Cohesive Bingham rheology: (a) Normal-integrated, (b) Integral and (c) differential basal resistance contributions. (i) Orthogonal mesh. (ii) Triangle structured mesh. (iii) Triangle unstructured mesh.

approaches show perfect circular spreading shapes, smooth free surface and final runout distances in agreement with those obtained in the orthogonal and the triangular structured meshes.

The comparison of the computational effort required for each integration procedure is summarized in Table 2. All the simulations are performed using a OMP-parallelized C++ code, running in four Intel Core i7-7700K CPU cores. Although differences in the required computational time appear depending on the mesh topology, the three integration procedures offer quite similar efficiency for each mesh type.

Based on these results, it is possible to conclude that both the integral

(b) and differential (c) approaches represent a further improvement for the explicit upwind integration of the non-Newtonian basal resistance contribution in two-dimensional numerical schemes.

### 6.3. Implicit centered vs. explicit upwind resistance: steady uniform flow of a frictional fluid

The goal of this benchmark test is to analyse the relative performance of the proposed explicit upwind and implicit centered strategies for the basal resistance discretization to converge to the exact solution in uniform steady flow. Under this regime, the system (10) reduces to  $\mathbf{S}_B(\mathbf{U}) = -\mathbf{S}_T(\mathbf{U})$ . Considering the Herschel-Bulkley relation (7) with behaviour exponent  $m = 2$  for the resistance and a uniform bed slope  $S$ , the components  $(u_\infty, v_\infty)$  of exact 2D velocity for the uniform steady flow can be calculated as

**Table 2**

Test 6.2.B – Computational time for the the three 2D basal resistance integration strategies considered.

Topology	Normal-int. procedure (a)	Integral approach (b)	Differential approach (c)
Orthogonal (SQ)	43.601 s	45.597 s	39.425 s
Triangle struct. (TS)	104.283 s	102.905 s	110.696 s
Triangle unstruct. (TU)	174.091 s	174.935 s	186.183 s

$$\begin{aligned} u_{\infty} &= \frac{S_x \sqrt{\rho g h_{\infty} - \frac{\tau_{f\infty}}{\sqrt{S_x^2 + S_y^2}}}}{\sqrt{\frac{25}{4} \frac{\mu p}{h_{\infty}^2} \sqrt{S_x^2 + S_y^2}}} \\ v_{\infty} &= \frac{S_y \sqrt{\rho g h_{\infty} - \frac{\tau_{f\infty}}{\sqrt{S_x^2 + S_y^2}}}}{\sqrt{\frac{25}{4} \frac{\mu p}{h_{\infty}^2} \sqrt{S_x^2 + S_y^2}}} \end{aligned} \quad (59)$$

with  $\tau_{f\infty} = (\rho - \rho_w) g h_{\infty} \tan \delta_f$ ,  $h_{\infty}$  the uniform flow depth and  $S_x = -\partial z_b / \partial x$  and  $S_y = -\partial z_b / \partial y$  the components of the uniform bed slope  $S$  along the  $x$ - and  $y$ -coordinates respectively.

#### Case 6.3.A: 1D framework uniform flow

First, we considered a 1D case with  $S_x = 0.07071$  and  $S_y = 0$ , i.e. bed slope only along the  $x$ -coordinate. Setting  $h_{\infty} = 1$  m,  $\rho = 2000$  kg/m<sup>3</sup>,  $\mu p = 10$  Pa·s<sup>2</sup> and  $\delta_f = 6^\circ$ , the exact velocity solution for the one-directional uniform flow is  $u_{\infty} = 2.38713$  m/s and  $v_{\infty} = 0$ , leading to a unit volume discharge  $q_{\infty} = h \sqrt{u_{\infty}^2 + v_{\infty}^2} = 2.38713$  m<sup>2</sup>/s. The initial conditions are set to  $\rho_0 = 2000$  kg/m<sup>3</sup>,  $h_0 = 5$  m,  $u_0 = -0.48$  m/s and  $v_0 = 0$ . At the inlet boundary, the inflow unit discharge is set to  $q_{\infty}$  whereas, at the outlet boundary, the flow depth is set to  $h_{\infty}$  during the simulation. This case is modelled using a 1D mesh of square cells with  $\Delta x = 1$  m. The CFL is set to 1 and the simulation runs until a steady state is reached.

Fig. 18 shows the exact depth and  $x$ -velocity solutions and the numerical results obtained using the two proposed strategies, integral and differential, for the explicit upwind discretization of the basal resistance term. Results obtained with the classical normal-integrated approach are also included. In the 1D case, the solutions obtained the three explicit upwind strategies converge to the exact uniform state. Regarding the implicit centered procedure for the basal resistance, the depth and velocity reach steady solutions but do not agree with the exact

uniform state values  $h_{\infty}$  and  $u_{\infty}$ . Therefore, only the explicit upwind formulations ensure the correct balance of conservative fluxes and source terms in steady state. This result agree with that reported by Burguete et al. (2008) for an equivalent implicit discretization method applied to the pure turbulent resistance term in 1D shallow water models.

#### Case 6.3.B: 2D framework uniform flow

The benchmark case is now extended to the 2D framework considering a spatial domain ( $x \in [0, 100]$  m,  $y \in [0, 100]$  m) where the bed slopes are  $S_x = 0.05$  and  $S_y = 0.05$ , i.e. the bed slope along the diagonal straight line  $x = y$  is  $|S| = \sqrt{S_x^2 + S_y^2} = 0.07071$  (see Fig. 19). Choosing  $h_{\infty} = 1$  m and the same fluid properties as in the previous case, the exact velocity solution for the uniform flow is  $u_{\infty} = 1.68796$  m/s and  $v_{\infty} = 1.68796$  m/s, leading to a unit volume discharge  $q_{\infty} = h \sqrt{u_{\infty}^2 + v_{\infty}^2} = 2.38713$  m<sup>2</sup>/s. The initial conditions are  $h_0 = 5$  m,  $u_0 = v_0 = 0.48$  m/s. During the simulation, at the inlet boundary (green rectangle in Fig. 19), the inflow unit discharge is set to  $q_{x\infty} = h_{\infty} u_{\infty}$  and  $q_{y\infty} = h_{\infty} v_{\infty}$  along the  $x$ - and  $y$ -coordinates respectively. At the outlet section (red rectangle in Fig. 19), the flow depth  $h_{\infty}$  is imposed as boundary condition. This case is modelled using a 2D triangular unstructured mesh of  $2 \cdot 10^4$  cells. The CFL is set to 1 and the simulation runs until a steady state is reached.

Fig. 20 depicts the 2D map of water depth  $h$  for the final steady state solution with (a) normal-integrated explicit upwind, (b) integral explicit upwind, (b) differential explicit upwind and (d) implicit centered methods for the discretization of the resistance term. First, note that all the methods show irregularities in the steady state solution, mainly caused by the irregular bed level integration derived from using a unstructured triangular mesh topology. Regardless of these irregularities, the classical explicit normal-integrated procedure does not converge to the exact uniform solution (see Fig. 20(a)). This loss of convergence of

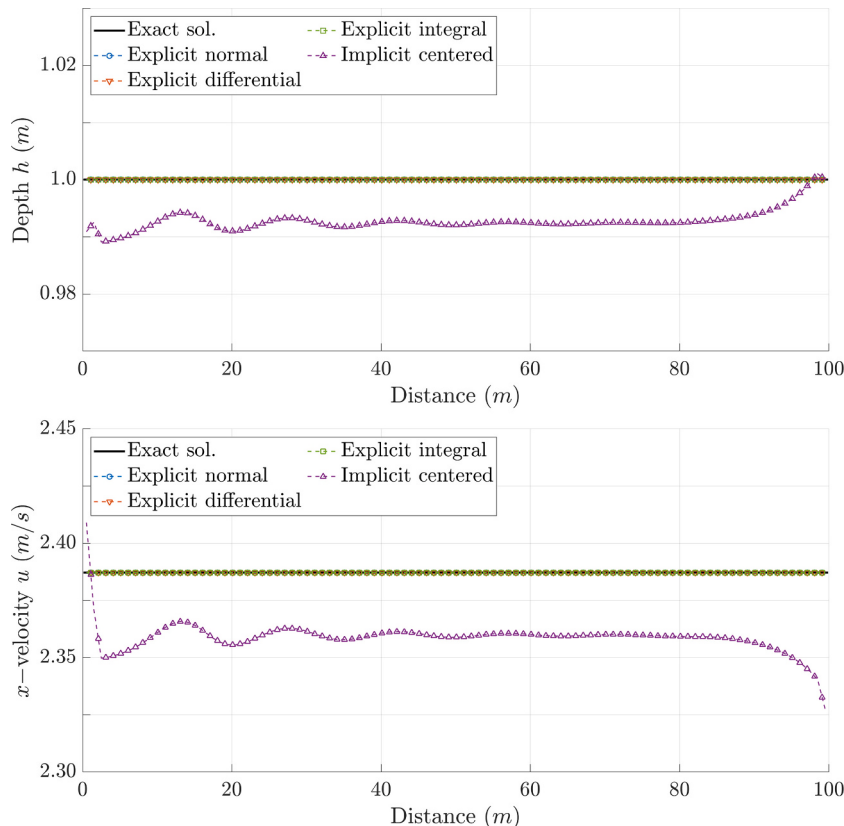
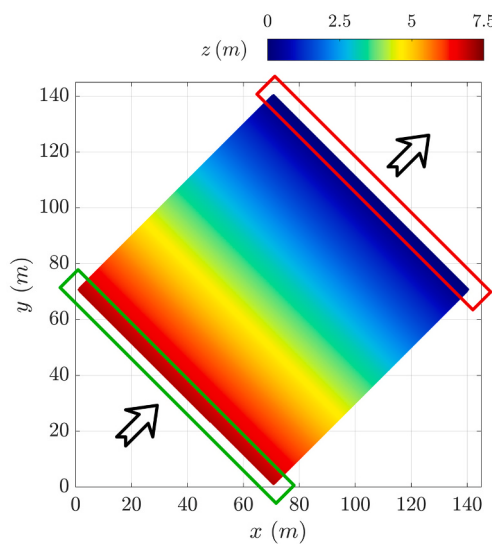


Fig. 18. Test 6.3.A – Convergence of the numerical solution for (top) the flow depth  $h$  and (bottom) the flow  $x$ -velocity  $u$  to the exact solution for the uniform steady state.



**Fig. 19.** Test 6.3.B – Bed level.

the classical method is caused by the high dependence of the integrated resistance force on the cell edge orientation and hence the loss of the invariance under rotation property.

Second, both the integral and the differential explicit upwind method tend to converge to a uniform flow solution (Figs. 20(b) and (c) respectively), but slightly different from the exact uniform state. The implicit centered method converges to a quasi-uniform flow but very different but also different from the exact solution (see Fig. 20(d)).

In order to perform a clear quantitative comparison, the solution obtained with each resistance discretization method has been averaged along the diagonal straight line  $x = y$ . Results are shown in Fig. 21 for (top) the averaged depth  $h$  and (bottom) the averaged velocity  $|\mathbf{u}|$  along the diagonal  $x = y$ . The best approximation to the exact uniform flow state is obtained with the differential explicit upwind method. The final steady solution using this method is uniform but shows a slightly lower velocity and a higher uniform depth than the exact values. Also the integral explicit upwind method underestimates slightly the velocity but the deviations in the flow depth with respect to the exact value are much larger than those using the differential method (see Fig. 21 top). Finally, the implicit centered method shows larger differences with respect to the exact uniform solution in both the flow depth  $h$  and velocity  $|\mathbf{u}|$ , specially close the inlet boundary, where only the unit discharge is imposed.

Two main conclusions can be extracted from this benchmark test: first, only the explicit upwind procedures for the integration of the basal resistance ensure the correct balance between conservative fluxes and momentum sources in steady states; and second, the differential explicit shows the best performance in the 2D framework involving steady

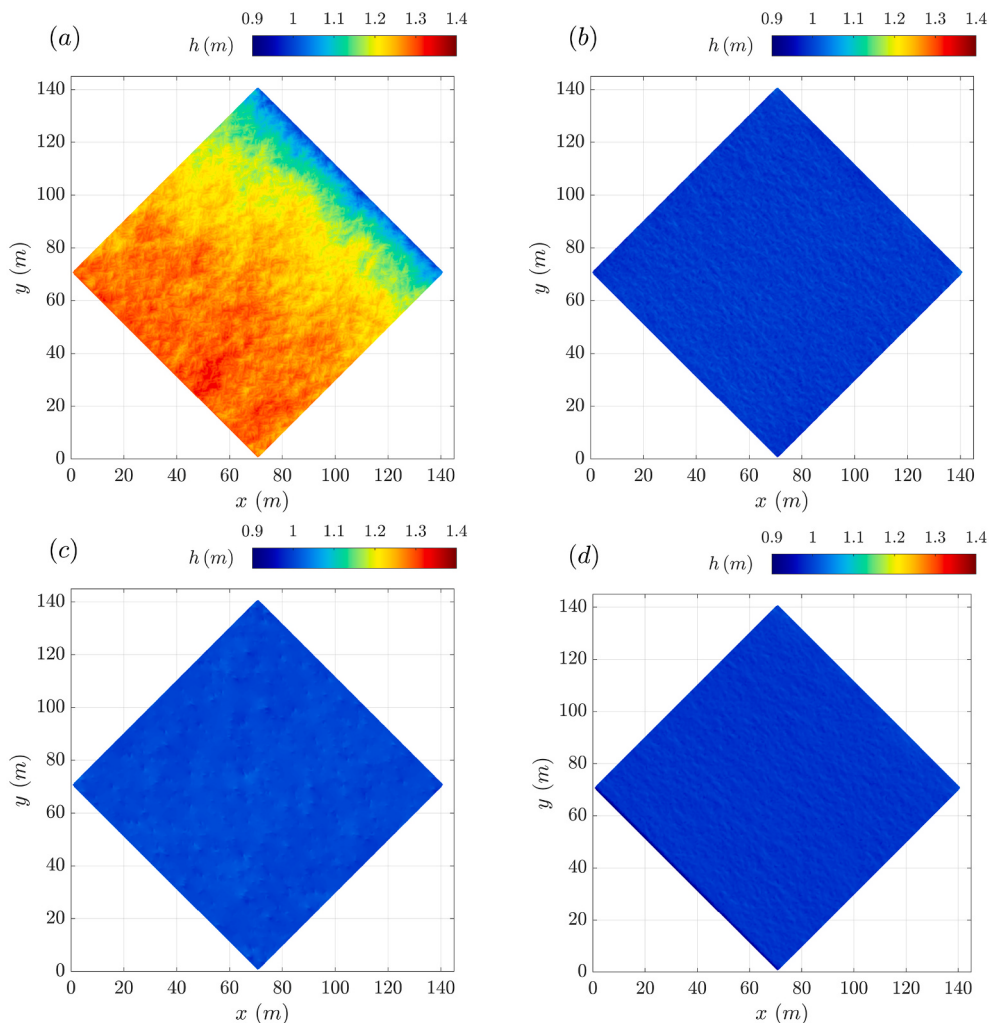


**Fig. 20.** Test 6.3.B – Water depth  $h$  for the final steady state solution with (a) normal-integrated explicit upwind, (b) integral explicit upwind, (c) differential explicit upwind and (d) implicit centered methods for the discretization of the resistance term.

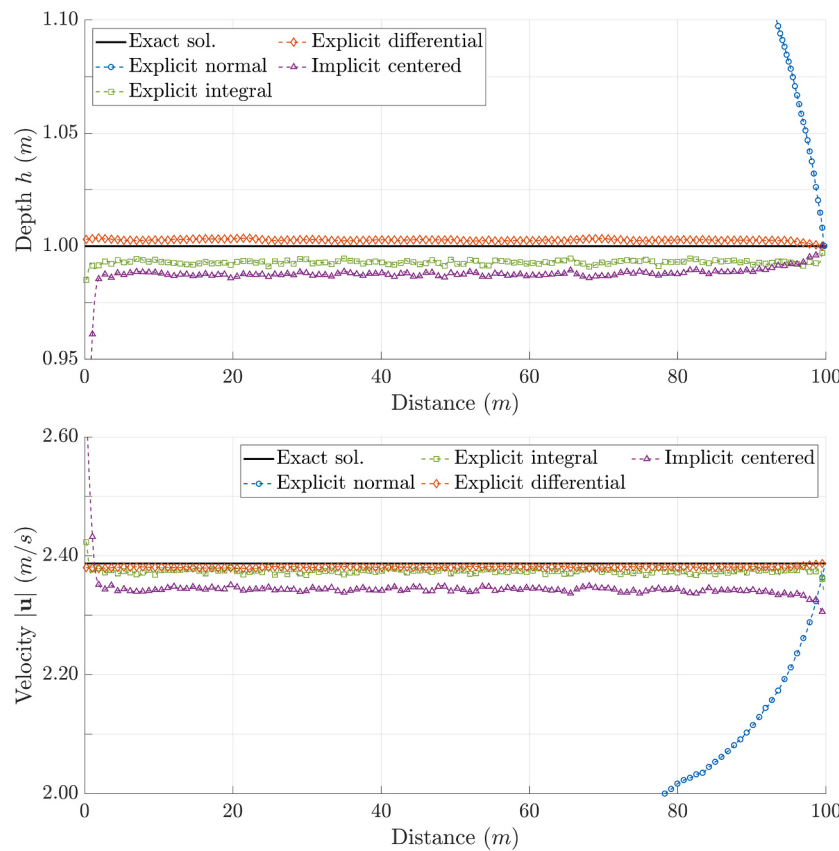


**Fig. 21.** Test 6.3.B – Convergence of the numerical solution for (top) the flow depth  $h$  and (bottom) the modulus of the velocity  $|\mathbf{u}|$  to the exact solution for the uniform steady state along the straight line  $x = y$ .

uniform regimes and unstructured meshes.

#### 6.4. Implicit centered vs. differential explicit upwind resistance: 2D circular dambreak of a frictional fluid

The goal of this test is to compare the implicit procedure proposed in this work for the centered integration of the basal resistance term against the differential explicit upwind method, dealing with two-dimensional non-Newtonian frictional transient flows. We aim to perform a quantitative comparison of the both strategies in terms of solution accuracy and robustness, as well as computational efficiency.

An axial-symmetric dambreak is considered within the flat bed domain ( $x \in [0, 500]$  m,  $y \in [0, 500]$  m), i.e. only the first quadrant is considered. The initial conditions are

$$\begin{aligned} h(x, y, 0) &= \begin{cases} 20 \text{ m} & \text{if } R \leq 100 \text{ m} \\ 2 \text{ m} & \text{if } R > 100 \text{ m} \end{cases} \\ u(x, y, 0) &= 0 \\ v(x, y, 0) &= 0 \end{aligned} \quad (60)$$

where  $R = \sqrt{x^2 + y^2}$  is the radius from the origin. The solid density is set to  $\rho_s = 3000 \text{ kg/m}^3$  with a uniform solid concentration  $\phi = 0.5$ , leading to a bulk density  $\rho = 2000 \text{ kg/m}^3$ . The plastic viscosity and the basal frictional angle for the quadratic non-linear model are set to  $\mu_p = 20 \text{ Pa}\cdot\text{s}^2$  and  $\delta_f = 2^\circ$  respectively. The spatial domain is discretized using five different orthogonal meshes, increasing progressively the refinement level (see Table 3). The time of flow is normalized using  $t^* = t \sqrt{g/h_0}$  and the final time simulated is  $t^* = 28$ , ensuring that the spreading wave does not reach the domain boundaries. A condition  $\text{CFL}=0.5$  is set, required for 2D orthogonal meshes. The results obtained

**Table 3**

Test 6.4 – 2D orthogonal meshes considered for the spatial discretization.

Mesh	Number of cells	Cell area	Edge length	Refin. level
M16	1024	256 m <sup>2</sup>	16 m	-
M8	3969	64 m <sup>2</sup>	8 m	×2
M4	15,625	16 m <sup>2</sup>	4 m	×2
M2	62,500	4 m <sup>2</sup>	2 m	×2
M1	250,000	1 m <sup>2</sup>	1 m	×2

with the finest mesh M1 are taken as reference.

Fig. 22(i) shows 3D views of the dambreak wave spreading at  $t^* = 28$  with the reference mesh M1 using (a) the differential explicit upwind and (b) the implicit centered methods for the discretization of the resistance term. Also the 2D map of the flow depth  $h$  is shown here. Furthermore, Fig. 22(ii) depicts the 2D map of the flow velocity  $|\mathbf{u}|$  at the normalized time  $t^* = 28$  using (a) the differential explicit upwind and (b) the implicit centered methods. Note that the wave spreading has not stopped yet and the velocity at the wave-front is still moderate. Both methods are able to maintain accurately the circular shape for the dambreak spreading wave, despite the orthogonal mesh topology is used. As in the above case, the alignment of the flow with the mesh main-directions reported by Pirulli et al. (2007) and Juez and Murillo (2013) does not appear using these new discretization procedures, and hence they ensure the rotation invariant property of the integrated basal resistance contribution.

Comparison of the flow depth  $h$  profile along the diagonal straight line  $x = y$  at  $t^* = 28$  shows that the solution obtained with the differential explicit upwind and the implicit centered methods in mesh M1 agree quite well (see Fig. 23(a)) and only small differences appear at the origin ( $x = 0, y = 0$ ) region. Furthermore, the time step evolution along

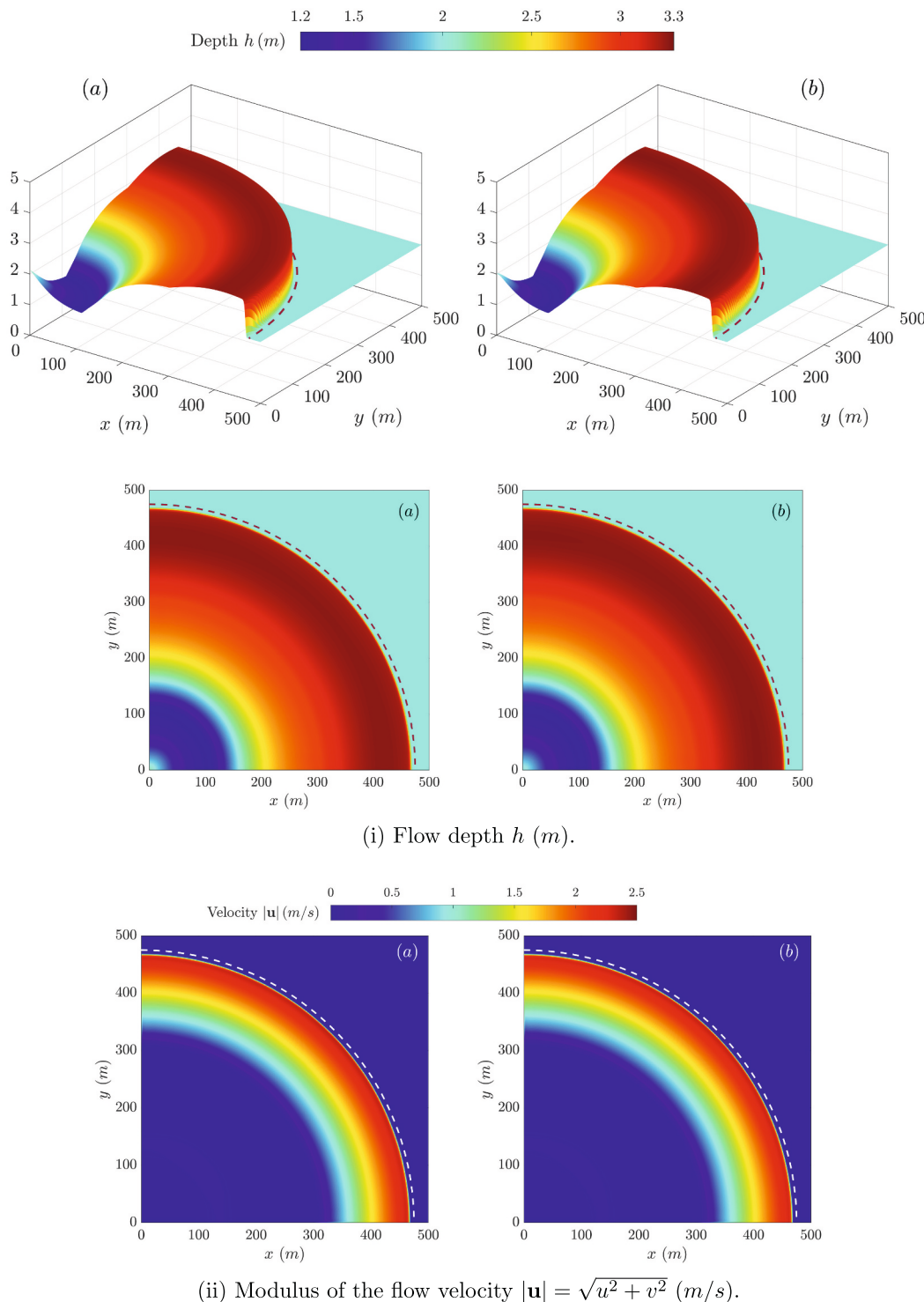


**Fig. 22.** Test 6.4 – Comparison of (a) differential explicit upwind and (b) implicit centered method for the resistance discretization with the reference mesh M1 at the normalized time  $t^* = 28$ . (i) Flow depth  $h$  (m). (ii) Modulus of the flow velocity  $|u| = \sqrt{u^2 + v^2}$  (m/s).

the simulation is depicted in Fig. 23(b). The dynamical minimum time step required for both methods for ensuring stability also agree perfectly. Moreover, Table 4 shows the computational effort required for both methods running in a single Intel Core i7-7700K CPU core and using mesh M1. This results demonstrate that both methods performs with a similar computational efficiency.

Finally, in order to demonstrate the convergence of the solution with the mesh refinement, Fig. 24 shows the profile of depth  $h$  along the diagonal straight line  $x = y$  using both (a) the differential explicit upwind

and (b) the implicit centered methods. For both procedures, the obtained result tends to the reference depth profile (with mesh M1) as the spatial discretization becomes finer. These results demonstrate the robustness and accuracy of the proposed procedures for the resistance discretization in the 2D framework.

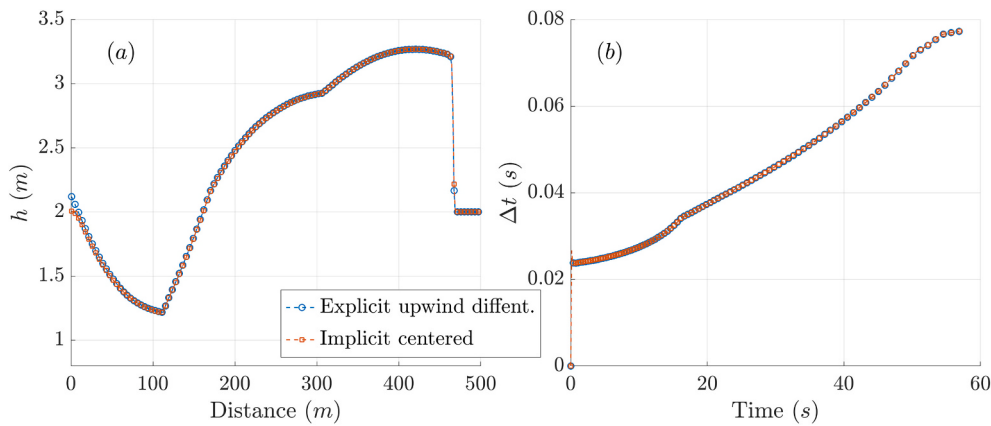


**Fig. 23.** Test 6.4 – (a) Flow depth  $h$  along the diagonal straight line  $x = y$  at  $t^* = 28$  and (b) minimum time step evolution for both the differential explicit upwind and the implicit centered methods with mesh M1.

**Table 4**

Test 6.4 – Computational time for both the differential explicit upwind and the implicit centered methods with mesh M1.

Mesh	(a) Differential explicit upwind	(b) Implicit centered
M1 Ref.	327.481 s	328.162 s

### 6.5. Realistic application: USGS debris dambreak experiments over rigid steep bed

In this benchmark case, the proposed strategies for the discretization of the basal resistance term are validated using data from a realistic experiment consisting of a dambreak flow of two-phase water-sediment fluidized material in a fixed bed large-scale steep channel. The

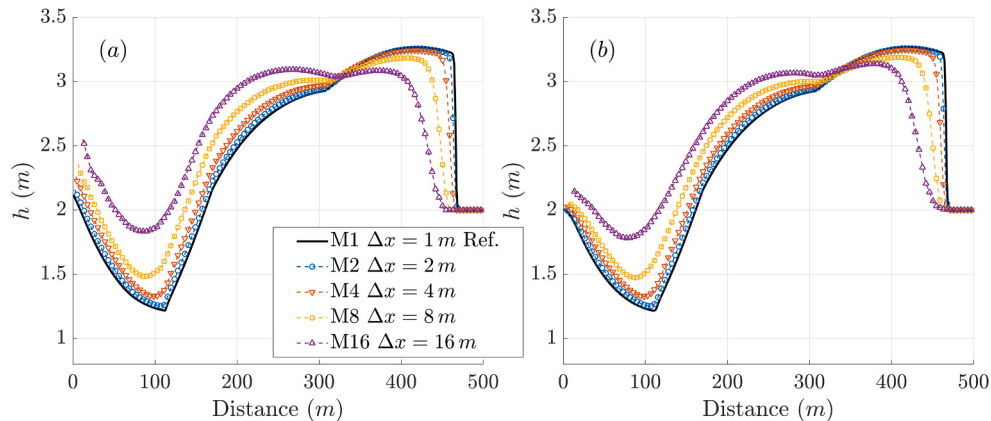


**Fig. 24.** Test 6.4 – Convergence of the flow depth  $h$  with the mesh refinement for (a) the differential explicit upwind and (b) the implicit centered resistance. Solution at the normalized time  $\bar{t} = 7$ .

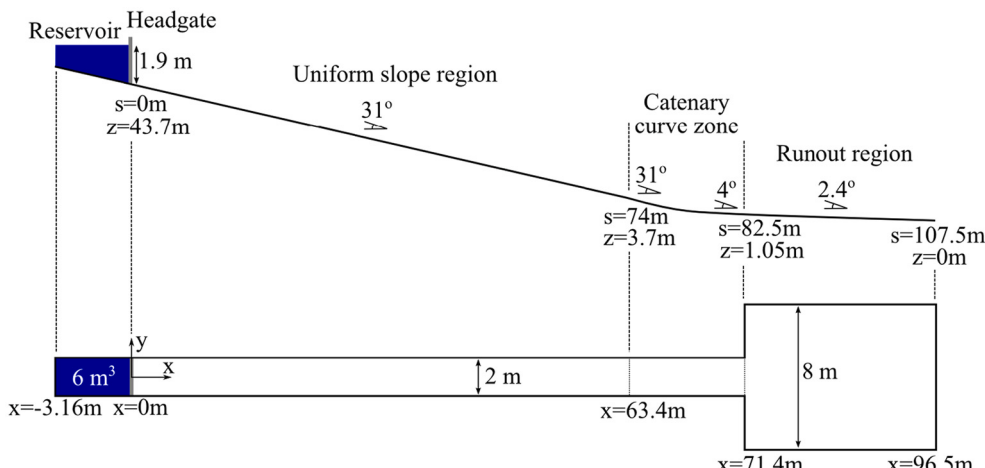


**Fig. 25.** Test 6.5 – Sketch of the USGS debris dambreak experiments.

experiment was carried out in the USGS large-scale debris-flow flume and data from two repetitions, called run I (date 12/9/2006) and J (date 19/6/2007), were reported by Iverson et al. (2011). The USGS debris-flow flume is a straight rectangular concrete channel 95 m long, 2 m wide and 1.2 m deep with a vertical headgate placed 12.5 m downstream the channel beginning, which retains the static debris fluid until the experiment upstream section. Fig. 25 shows a schematic representation of the USGS debris-flow flume for this experiments. All the longitudinal distances  $s$  are referred to the headgate position and taken along the experimental flume floor. The channel has an  $31^\circ$  uniform slope until  $s = 74$  m, where the flume begins to flatten following a catenary curve and evolving to a  $4^\circ$  slope at  $s = 82.5$  m. Then, the flume debouches onto a 15 m long, 8 m wide and  $2.4^\circ$  slope concrete runout surface.

In the experiments, once the headgate was opened, the debris dam-break wave accelerated over the uniform-slope rigid bed region of the flume until it reached the catenary-slope zone and the runout surface, where it stopped. For each run of the experiment, Iverson et al. (2011) tracked the wave-front location during the flow advance using image techniques and video frames. Video files of both experiments are available in <https://pubs.usgs.gov/of/2007/1315/>.

The characteristics of the debris aggregate were previously reported in Iverson et al. (2010). The initial debris volume was  $6 \text{ m}^3$  and was composed by a fully saturated mixture of water and gravel, sand and mud grains with 60% bulk solid concentration. For the sake of simplicity, the characteristic diameter of the solid particles is taken as  $d_s = 6.9 \text{ mm}$ , the solid density is  $\rho_s = 2700 \text{ kg/m}^3$  and the pore-fluid density is assumed as  $\rho_w = 1000 \text{ kg/m}^3$ , leading to an initially uniform bulk density  $\rho = 2020 \text{ kg/m}^3$ . Table 5 shows the main parameter used in the simulations for characterizing the debris mixture.

The frictional Herschel-Bulkley model (7) is chosen for modeling the basal shear stress. The behavior index is set to  $m = 2$  in order to allow the application of the implicit centered strategy. The basal effective frictional angle is set to  $\delta_f = 2.5^\circ$ , allowing the detention at the runout region, and the plastic viscosity parameter is calibrated to  $\mu_p = 0.1 \text{ Pa}\cdot\text{s}^2$ . The simulations are performed using an unstructured triangular mesh of 28,388 cells, with an averaged area of  $200 \text{ cm}^2$ . The CFL is set to 0.95 and the total duration simulated is  $t_{end} = 30 \text{ s}$ .

Fig. 26 shows the computed depth of the debris wave at different times after the flow beginning using the explicit upwind differential procedure for the discretization of the basal resistance term. The other discretization strategies show a similar behavior. Note that the distances are expressed in the horizontal  $x$ - and  $y$ -coordinates. Analyzing the behavior of the computational solution, after the flow initialization, the dam-break wave moves downslope rapidly creating a marked main wave front (Fig. 26(a)). As this main wave progresses, the debris material undergoes increasing shearing states as it accelerates over the steep channel. These increasing shear rates are associated to the appearance of secondary roll waves behind the main wave front (Fig. 26(b)). Note that these roll waves were also observed in the experiments. Then, the main wave reaches the catenary zone and the runout region, where it stops (Fig. 26(c)), whereas secondary roll waves continue appearing at the step region and increasing progressively the runout distance as they move downslope (Fig. 26(d)).

Fig. 27 depicts the numerical front location along the experimental

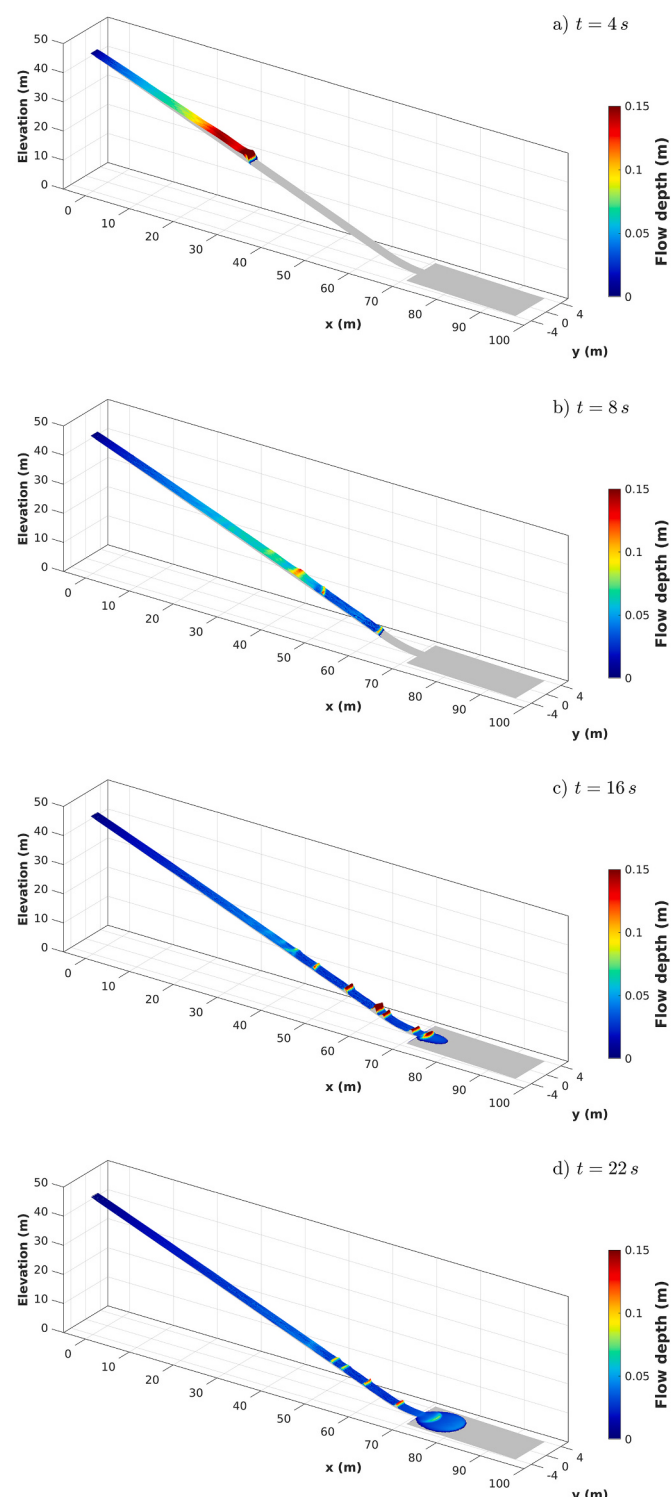


**Fig. 26.** Test 6.5 – 3D view of the dam-break debris flow evolution at (a)  $t = 4 \text{ s}$ , (b)  $t = 8 \text{ s}$ , (c)  $t = 16 \text{ s}$  and (d)  $t = 24 \text{ s}$ .

channel as time progresses with the four different discretization strategies analyzed in this work. The numerical results are compared with the provided experimental data. First, note that the numerical model is able to predict reasonably well the advance of the dam-break wave front along the steep channel, as well as the flow detention at the runout region, regardless of the discretization strategy. Second, the explicit upwind integral, the explicit upwind differential and the implicit centered strategies for resistance term discretization show quite similar results in

**Table 5**  
Test 6.5 – Characteristic values used for the simulation.

Debris volume	$6 \text{ m}^3$
Bulk solid concentration $\phi$	60%
Bulk debris density $\rho$	$2020 \text{ kg/m}^3$
Pore-fluid density $\rho_w$	$1000 \text{ kg/m}^3$
Basal effective angle $\delta_f$	$2.5^\circ$
Behavior index $m$	2
Plastic viscosity $\mu_p$	$0.1 \text{ Pa}\cdot\text{s}^2$

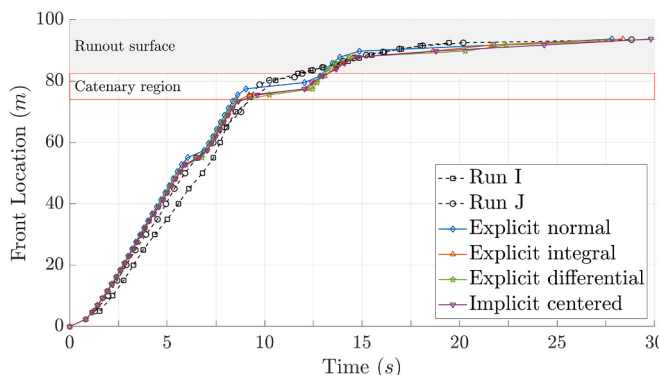


Fig. 27. Test 6.5 – Temporal evolution of the dambreak wave front location.

terms of wave-front advance. These similar results for this complex highly unsteady benchmark case demonstrate the consistence of the novel strategies proposed for the treatment of the basal resistance force. Nevertheless, the explicit normal-integrated approach shows more marked differences respect to the other strategies, specially at the catenary region where the flow velocity decreases suddenly. It is noteworthy that, in this realistic case, preferred main-directions do not appear in the flow with the normal-integrated strategy because of the unstructured triangular mesh used.

Regarding the numerical stability of the proposed discretization strategies, Fig. 28 depicts the dynamic time step evolution during the simulation each 25 interactions. The three explicit upwind approaches, as well as the implicit centered procedure, show a quite similar time step limitation during most of the simulated event duration. Only when the flow is stopping at the runout region ( $t > 20$  s), the implicit procedure allows a slightly higher time step than the explicit approaches. It is worth mentioning that the proposed explicit upwind strategies do not require additional time step restrictions to ensure the numerical stability of the solution, despite the used  $CFL = 0.95$  is close to the stability threshold  $CFL = 1$ . Finally, Table 6 shows the computational effort required by the proposed discretization strategies. The implicit centered approach is slightly faster than the explicit upwind procedures for this test but not important differences can be found.

## 7. Conclusions

In this work, different strategies for the discretization of the 2D non-Newtonian basal resistance term in depth-averaged shallow flow models have been proposed and analysed. First, two new methods for the explicit upwind discretization have been derived. These novel approaches, called integral and differential methods respectively, ensure that the property of rotation invariance for the net integrated resistance

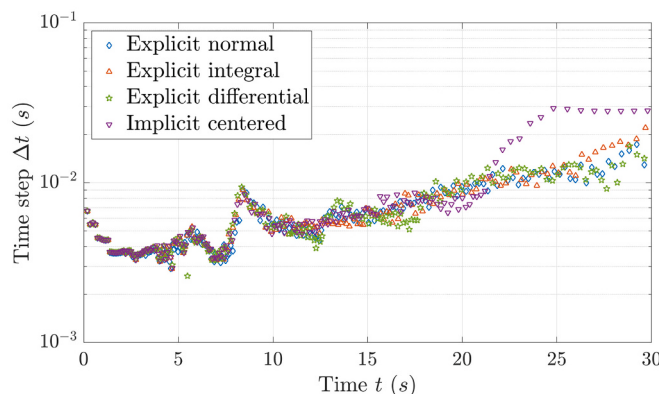


Fig. 28. Test 6.5 – Dynamic time step  $\Delta t$  during the dambreak flow simulation.

Table 6

Test 6.5 – Computational time required and speed up of the proposed discretization strategies.

Discretization	Computational time	Speed-up
Normal-integrated explicit upwind	71.648	–
Integral explicit upwind	70.221	1.0203
Differential explicit upwind	69.295	1.0340
Implicit centered	63.044	1.1365

force is satisfied in any 2D mesh topology. Orthogonal, triangular structured and triangular unstructured meshes have been tested in this work. For the sake of completeness, these new explicit upwind strategies have been compared with the previous method for the integration of the friction terms at the cell edges in non-Newtonian shallow-flow models, referred to as normal-integrated method here.

Furthermore, a novel implicit centered method for the integration of the 2D resistance force has also been derived for the quadratic frictional non-linear shear stress formulation. This new implicit strategy allows to compute the updated mass rate using a non-iterative formulation based only on the known values of conservative variables at the current time. This new implicit centered strategy has been compared with the explicit upwind strategies for predicting steady and transient frictional flows.

First, the explicit procedures for the upwind resistance integration have been faced to an one-directional dambreak of a cohesive Bingham fluid. When a 1D mesh of squared cells is used, the proposed integral and differential methods reduce to the same solution. However, if the spatial domain is discretized using a 2D mesh, the classical normal-integrated method shows a high dependence on the mesh topology. Contrarily, the results obtained using the proposed integral and differential explicit upwind procedures does not depends on the mesh type. Furthermore, the 2D solution using the differential upwind method converges exactly to the result obtained with the 1D mesh.

Second, the explicit procedures have been tested against a large-scale 2D spreading of a non-Newtonian cylinder. Both the frictional non-linear and cohesive Bingham formulations have been used in this benchmark test running in orthogonal, triangle structured and triangle unstructured meshes. Results show that using the classical normal-integrated method leads to the appearance of marked preferential directions in the flow aligned with the mesh axis. This behavior was previously reported by Pirulli et al. (2007) and Juez and Murillo (2013) but it was erroneously attributed to an insufficient mesh refinement. Nevertheless, this large-scale numerical experiment shows that the alignment of the flow with the mesh axis is directly related to the loss of the rotation invariance for the integrated resistance force, caused by the erroneous procedure for including the 2D resistance term into the local plane RP at the cell edges. Contrarily, both the novel integral and differential explicit upwind approaches derived in this work maintain approximately the circular shape for the spreading wave until the flow detention, with as quite similar runout distance.

Then, the capability of the three explicit upwind methods for converging to steady flow states is tested in the 1D and 2D framework. Moreover, the novel implicit centered method for quadratic frictional Herschel-Bulkley fluids has also been tested. In the 1D framework, the proposed integral and differential explicit upwind procedures converges accurately to the exact solution for the steady uniform flow, as well as the classical normal-integrated method. Nevertheless, the solution using the implicit centered strategy converges to a steady state slightly different from the exact uniform flow. Furthermore, when the test is extended to the 2D framework, the classical normal-integrated upwind method does not converge to a uniform solution due to the dependence on the 2D mesh topology. The integral and differential explicit methods converge to a steady uniform state close to the exact solution, whereas the implicit centered strategy shows a less accurate solution. The best result is obtained with the differential explicit upwind procedure.

The implicit centered procedure is faced to the differential explicit

upwind method dealing with two-dimensional non-Newtonian frictional transient flows. An axial-symmetric dambreak is considered within the flat bed domain discretized using orthogonal meshes with different refinement. We perform a quantitative comparison of the both strategies in terms of solution accuracy and robustness, as well as computational efficiency. Both methods are able to maintain accurately the circular shape for the dambreak spreading wave, avoiding the alignment of the flow with the mesh orthogonal directions. Moreover the solution obtained with the differential explicit upwind and the implicit centered methods agree quite well, showing similar mesh convergence and computational efficiency.

Finally, the implicit centered and the three explicit upwind strategies have been faced to the large-scale debris dambreak experiments over rigid steep bed carried out by the US Geological Survey in order to study the numerical stability of the proposed strategies dealing with realistic unsteady complex flows. The explicit upwind integral, the explicit upwind differential and the implicit centered strategies show quite similar results, demonstrating the consistence of the novel strategies proposed in this work. Nevertheless, the explicit normal-integrated approach shows more marked differences respect to the other strategies. Furthermore, the proposed explicit upwind strategies do not require further time step restrictions to ensure the numerical stability of the solution.

Based on these results, it is possible to conclude that both the integral

and differential explicit upwind approaches represent a further improvement for the integration of generalized non-Newtonian resistance terms in numerical schemes for 2D complex shallow flows.

#### CRediT authorship contribution statement

**S. Martínez-Aranda:** Conceptualization, Methodology, Software, Validation, Writing – original draft, Writing – review & editing. **J. Murillo:** Conceptualization, Methodology, Writing – review & editing. **M. Morales-Hernández:** Conceptualization, Methodology, Writing – review & editing. **P. García-Navarro:** Project administration, Resources, Supervision, Writing – review & editing.

#### Declaration of Competing Interest

The authors declare that they have no known competing financial interests or personal relationships that could have appeared to influence the work reported in this paper.

#### Acknowledgements

This work was partially funded by the MINECO/FEDER under research project PGC2018-094341-B-I00 and by Diputación General de Aragón, DGA, through Fondo Europeo de Desarrollo Regional, FEDER.

## Appendix A. Closure relations for viscoplastic basal resistance

### A.1. Viscoplastic Bingham model

The widespread linear viscoplastic relation, also called Bingham model, can be used to estimate the stress distribution in laminar simple-shear flows of cohesive viscous materials as:

$$\tau(z) = \tau_y + \mu_B \frac{dU}{dz} \quad (61)$$

where  $\tau_y$  [Pa] is a pure cohesive yield stress for the motion initiation,  $\mu_B$  [Pa·s] accounts for the bulk viscosity of the material and  $U$  denotes the modulus of the local flow velocity.

Assuming simple-shear stress, the flow structure consists of the two separate regions depicted in Fig. 29. For  $z_0 < z \leq z_s$ , the induced shear stress along the flow direction  $\tau(z)$  is lower than the yield strength  $\tau_y$ , hence the velocity is constant throughout the plug region. In the lower region ( $z_b < z \leq z_0$ ), the induced shear stress is larger than  $\tau_y$  and the material is sheared.

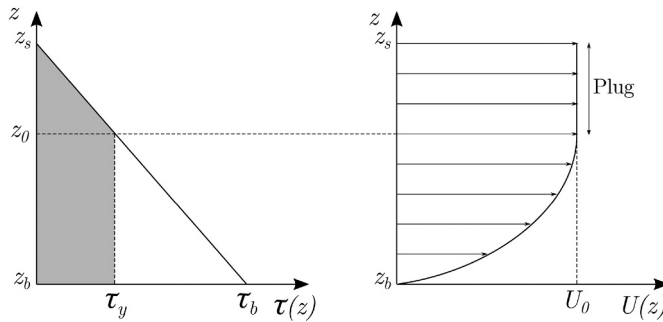


Fig. 29. Velocity and stress distribution for the Bingham model.

The induced shear stress can be expressed as

$$\tau(z) = \tau_b \left( 1 - \frac{z - z_b}{h} \right) \quad (62)$$

and, using (61), the velocity derivative in the shearing region reads

$$\frac{dU}{dz} = \frac{1}{\mu_B} (\tau(z) - \tau_y) \quad (63)$$

Replacing (62) into (63) and integrating throughout the shearing region  $z_b < z \leq z_0$  allows to obtain the velocity profile for the entire flow column as

$$U(z) = \begin{cases} \frac{\tau_b - \tau_y}{\mu_B} (z - z_b) - \frac{\tau_b}{2\mu_B h} (z - z_b)^2 & \text{if } z_b < z \leq z_0 \\ U_0 & \text{if } z_0 < z \leq z_s \end{cases} \quad (64)$$

being  $z_0$  the elevation of the shearing region and  $U_0$  the velocity of the plug region, expressed as

$$z_0 = z_b + h \left( 1 - \frac{\tau_y}{\tau_b} \right) \quad U_0 = \frac{\tau_b h}{2\mu_B} \left( 1 - \frac{\tau_y}{\tau_b} \right)^2 \quad (65)$$

Integrating (64) throughout the flow column leads to a cubic equation

$$\left( \frac{\tau_y}{\tau_b} \right)^3 - \left( 3 + \frac{6\mu_B \bar{U}}{\tau_y h} \right) \frac{\tau_y}{\tau_b} + 2 = 0 \quad (66)$$

which relates the basal shear stress  $\tau_b$ , the yield strength  $\tau_y$  and the depth-averaged flow velocity  $\bar{U} = \sqrt{u^2 + v^2} = |\mathbf{u}|$ . Note that (66) can be rewritten as

$$2\tau_b^3 - 3 \left( \tau_y + 2\mu_B \frac{|\mathbf{u}|}{h} \right) \tau_b^2 + \tau_y^3 = 0 \quad (67)$$

which can be analytically solved to obtain the basal resistance  $\tau_b$  as a function of the flow depth and depth-averaged velocity.

#### A.2. Frictional Herschel-Bulkley model

The non-linear viscoplastic model combined with a Coulomb-Terzaghi yield strength can be used for modeling flows of liquid-solid mixtures where the intergranular frictional stresses are important. For this constitutive model, also called frictional Herschel-Bulkley model, the shear stress distribution along the flow column reads

$$\tau(z) = \sigma_e(z) \tan \delta_f + \mu_P \left( \frac{dU}{dz} \right)^m \quad (68)$$

where  $\sigma_e(z)$  [Pa] is the effective normal stress distribution,  $\delta_f$  accounts for the effective frictional angle between solid grains,  $\mu_P$  [Pa·s<sup>m</sup>] is the plastic viscosity coefficient,  $U$  denotes the modulus of the local flow velocity and  $m$  is the behavior index.

If the pore-fluid pressure distribution in the flow column is considered hydrostatic, the yield stress distribution can be estimated as

$$\begin{aligned} \sigma_e(z) \tan \delta_f &= [\sigma(z) - \mathcal{P}(z)] \tan \delta_f \\ &= \left[ \rho g h \left( 1 - \frac{z - z_b}{h} \right) - \rho_w g h \left( 1 - \frac{z - z_b}{h} \right) \right] \tan \delta_f \end{aligned} \quad (69)$$

where  $\sigma(z_b) = \rho g h$  and  $\mathcal{P}(z_b) = \rho_w g h$  represent the total normal stress and the hydrostatic pore pressure at the bed surface respectively (Fig. 30). Hence the constitutive Eq. (68) can be rewritten as

$$\tau(z) = \tau_f \left( 1 - \frac{z - z_b}{h} \right) + \mu_P \left( \frac{dU}{dz} \right)^m \quad (70)$$

being  $\tau_f$  the value of the frictional yield strength at the basal surface, expressed as

$$\tau_f = (\rho - \rho_w) g h \tan \delta_f \quad (71)$$

As in the Bingham model, we assume the simple shear distribution

$$\tau(z) = \tau_b \left( 1 - \frac{z - z_b}{h} \right) \quad (72)$$

which, replacing (72) into (70), allows to express the local velocity derivative along the flow column as

$$\frac{dU}{dz} = \left[ \frac{\tau_b - \tau_f}{\mu_P} \left( 1 - \frac{z - z_b}{h} \right) \right]^{1/m} \quad (73)$$

and integrating (73) leads to the velocity vertical distribution

$$U(z) = \frac{m}{m+1} \left( \frac{\tau_b - \tau_f}{\mu_P} \right)^{1/m} h \left[ 1 - \left( 1 - \frac{z - z_b}{h} \right)^{\frac{m+1}{m}} \right] \quad (74)$$

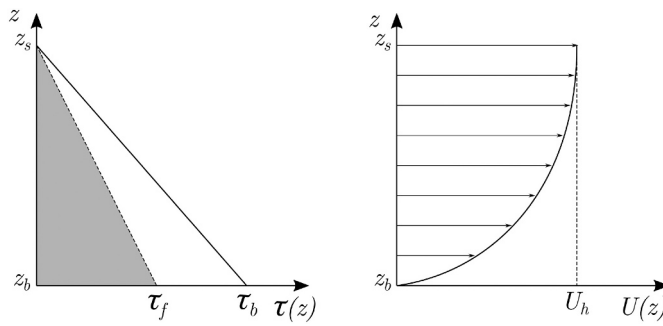


**Fig. 30.** Velocity and stress distribution for the frictional Herschel-Bulkley model.

Note that the velocity at the free surface can be expressed as

$$U(z_s) \equiv U_h = \frac{m}{m+1} \left( \frac{\tau_b - \tau_f}{\mu_p} \right)^{1/m} h \quad (75)$$

Finally, integrating (74) throughout the flow column leads to

$$\bar{U} = \frac{m+1}{2m+1} U_h \quad (76)$$

which relates the depth-averaged flow velocity  $\bar{U} = \sqrt{u^2 + v^2} = |\mathbf{u}|$  to the free surface velocity  $U_h$  and allows to obtain the basal shear stress  $\tau_b$  as

$$\tau_b = \tau_f + \left( \frac{2m+1}{m} \right)^m \mu_p \left( \frac{|\mathbf{u}|}{h} \right)^m \quad (77)$$

It is worth mentioning that (77) represents a generalized depth-integrated formulation for viscoplastic flows which encompasses:

- Shear-thinning behavior for  $m < 1$ , reducing the apparent viscosity as the induced shear rate increases. Taking  $m = 0.5$  leads to

$$\tau_b = \tau_f + \left( \sqrt{2} \mu_p \dot{\gamma}^{-1/2} \right) \dot{\gamma} \quad (78)$$

being  $(\sqrt{2} \mu_p \dot{\gamma}^{-1/2})$  the apparent viscosity and  $\dot{\gamma} = 2 \frac{|\mathbf{u}|}{h}$  the macroscopic shear rate.

- Linear viscoplastic behavior for  $m = 1$ , with a linear relation between shear stress and shear rate following

$$\tau_b = \tau_f + \left( \frac{3}{2} \mu_p \right) \dot{\gamma} \quad (79)$$

with a constant apparent viscosity  $\left( \frac{3}{2} \mu_p \right)$ .

- Shear-thickening behavior for  $m > 1$ , increasing the apparent viscosity as the induced shear rate grows. Taking  $m = 2$  leads to

$$\tau_b = \tau_f + \left( \frac{25}{16} \mu_p \dot{\gamma} \right) \dot{\gamma} \quad (80)$$

where  $\left( \frac{25}{16} \mu_p \dot{\gamma} \right)$  is the apparent viscosity.

## Appendix B. Frictionless upwind flux computation

In this work, this frictionless flux vector is upwind computed using the approximate Riemann problem (RP) theory and a first-order Roe's solver for compressible shallow flows. Details on the flux computation have been extensively reported in Martínez-Aranda et al. (2021), Martínez-Aranda et al. (2020), Martínez-Aranda (2021) but, for the sake of completeness, a summary is included here. The frictionless flux vector  $\mathbf{F}_k^\downarrow$  at the  $k$ th cell edge, separating the left  $i$  cell and the right  $j$  cell, is expressed as

$$\mathbf{F}_k^\downarrow = \mathbf{F}(\hat{\mathbf{U}}_i^n, \hat{\mathbf{U}}_j^n)_k - \mathbf{H}(\hat{\mathbf{U}}_i^n, \hat{\mathbf{U}}_j^n)_k \quad (81)$$

and its computation is based on the conservative Jacobian  $\tilde{\mathbf{J}}_k(\hat{\mathbf{U}}_i^n, \hat{\mathbf{U}}_j^n)$ , defined as

$$\tilde{J}_k = \begin{pmatrix} 0 & 1 & 0 & 0 \\ \frac{1}{2}g_n\tilde{h}(1+\tilde{r}) - \tilde{u}_n^2 & 2\tilde{u}_n & 0 & -\frac{1}{2}g_n\tilde{h}\tilde{r} \\ -\tilde{u}_n \tilde{v}_t & \tilde{v}_t & \tilde{u}_n & 0 \\ -\tilde{u}_n \tilde{\phi}^\times/\tilde{r} & \tilde{\phi}^\times/\tilde{r} & 0 & \tilde{u}_n \end{pmatrix}_k \quad (82)$$

where the  $\tilde{h}$  is the edge-averaged flow depth,  $\tilde{r}$  is the edge-averaged bulk density,  $\tilde{\phi}^\times$  is the edge-averaged buoyant solid and  $(\tilde{u}_n, \tilde{v}_t)$  are the edge-averaged normal and tangential velocity, respectively, to the  $k$ th cell edge.

The approximate matrix  $\tilde{J}_k$  (82) has four different real eigenvalues

$$\tilde{\lambda}_{1,k} = (\tilde{u}_n - \tilde{c})_k \quad \tilde{\lambda}_{2,k} = (\tilde{u}_n)_k \quad \tilde{\lambda}_{3,k} = (\tilde{u}_n + \tilde{c})_k \quad \tilde{\lambda}_{4,k} = (\tilde{u}_n)_k \quad (83)$$

being  $\tilde{c}_k$  the edge-averaged celerity, defined as

$$\tilde{c}_k = \left( \sqrt{\frac{1}{2}g_n\tilde{h}(1+\tilde{r}-\tilde{\phi}^\times)} \right)_k \quad (84)$$

and allowing to diagonalize the matrix as  $\tilde{J}_k = (\tilde{P}\tilde{\Lambda}\tilde{P}^{-1})_k$ , where  $\tilde{\Lambda}_k$  is a diagonal matrix containing the eigenvalues  $\lambda_{m,k}$ , the matrix  $\tilde{P}_k = (\tilde{e}_1, \tilde{e}_2, \tilde{e}_3, \tilde{e}_4)_k$  contains the orthogonal basis of eigenvectors  $(\tilde{e}_m)_k$  and  $\tilde{P}_k^{-1}$  denotes its inverse matrix.

According the Roe linearisation, the numerical frictionless flux at the  $k$ th cell edge  $F_k^\downarrow$  is provided by a discontinuous flux function constructed by defining appropriate Rankine-Hugoniot (RH) relations across each moving wave  $\lambda_{m,k}$ . The upwind value of the frictionless flux vector for the  $i$  cell can be computed as

$$F_k^{\downarrow-} = F(\hat{U}_i^n) + \sum_{m-} [(\tilde{\lambda}_m \tilde{\alpha}_m - \tilde{\beta}_m) \tilde{e}_m]_k^n \quad (85)$$

where the subscript  $m-$  under the sums indicate waves travelling inward the  $i$  cell. The coefficients  $\tilde{\alpha}_{m,k}$  denotes the wave strengths accounting for the discontinuity on the conservative variables between cell center,  $\hat{U}_j^n - \hat{U}_i^n$ , and the coefficients  $\tilde{\beta}_{m,k}$  are the source strengths which include the integrated bed pressure contribution through the cell edge,  $H(\hat{U}_i^n, \hat{U}_j^n)_k = (0, -g_n\tilde{r}\tilde{h}\Delta z_b, 0, 0)_k^T$ , both satisfying

$$\hat{U}_j^n - \hat{U}_i^n = \sum_{m=1}^4 (\tilde{\alpha}_m \tilde{e}_m)_k^n \quad (86a)$$

$$H(\hat{U}_i^n, \hat{U}_j^n)_k = \sum_{m=1}^4 (\tilde{\beta}_m \tilde{e}_m)_k^n \quad (86b)$$

Note that the frictionless mass rates at the time  $t = t^n$  along the normal and tangential directions to the  $k$ th cell edge, called  $(m_n, m_t)_k$  respectively, can be computed using the properties of the approximate RP solution as

$$(m_n)_k = (rh_u)_i^n + \sum_{m-} [\tilde{\lambda}_m \tilde{\alpha}_m - \tilde{\beta}_m]_k^n$$

$$(m_t)_k = (rh v_i)_i^n + \sum_{m-} \left[ \frac{\tilde{v}_t}{\tilde{\lambda}_m} \left( \tilde{\lambda}_m \tilde{\alpha}_m - \tilde{\beta}_m \right) \right]_k^n \quad (87)$$

Finally, in order to ensure the stability of the explicitly computed numerical solution, the time step should be small enough to avoid the interaction of waves from neighbouring Riemann problems. The dynamical limitation of the time step at each  $k$  edge is addressed here assuming that the fastest wave celerity corresponds to the absolute maximum of the eigenvalues of  $\tilde{J}_k$  (82) as

$$\Delta t_k = \frac{\min(A_i, A_j)}{l_k \max(|\tilde{\lambda}_{1,k}|, |\tilde{\lambda}_{3,k}|)} \quad (88)$$

and the global time step  $\Delta t = t^{n+1} - t^n$  is limited using the Courant-Friedrichs-Lowy (CFL) condition

$$\Delta t = \text{CFL} \min_k(\Delta t_k) \quad (89)$$

with  $\text{CFL} < 0.5$  for square orthogonal meshes and  $\text{CFL} < 1$  for the triangular mesh topology and 1D-mesh cases

### Appendix C. Derivation of the implicit centered method for the resistance discretization

The basal resistance  $\tau_b$  for the frictional non-linear visco-plastic model with behaviour exponent  $m = 2$  can be expressed as

$$\tau_b = \tau_b n_u = \tau_f \frac{rh_u}{|rh_u|} + \frac{25}{4} \mu_p \frac{|rh_u| rh_u}{(rh)^2 h^2} \quad (90)$$

where  $rhu$  is the normalized mass rate in the global horizontal coordinate system  $\mathbf{X} = (x, y)$ . Considering an implicit centered scheme for the basal resistance contribution, the updating formula is written as

$$\mathbf{U}_i^{n+1} = \mathbf{U}_i^n - \frac{\Delta t}{A_i} \sum_{k=1}^{\text{NE}} \mathbf{R}_k^{-1} \mathbf{F}_k^{\downarrow} l_k + \Delta t S_r(\mathbf{U}_i^{n+1}) \quad (91)$$

with  $\mathbf{F}_k^{\downarrow} = (F_1, F_2, F_3, F_4)_k^{\downarrow}$  and the conservative variables are computed as

$$(rh)^{n+1}_i = (rh)^n_i - \frac{\Delta t}{A_i} \sum_{k=1}^{\text{NE}} (F_1)_k^{\downarrow} l_k \quad (92a)$$

$$(rhu)^{n+1}_i = (rhu)^n_i - \frac{\Delta t}{A_i} \sum_{k=1}^{\text{NE}} (F_2 n_x - F_3 n_y)_k^{\downarrow} l_k - \Delta t \left( \frac{\tau_f}{\rho_w} \frac{|rhu|}{|rhu|} + \frac{25}{4} \frac{\mu_p}{\rho_w} \frac{|rhu| rhu}{(rh)^2 h^2} \right)_i^{n+1} \quad (92b)$$

$$(rvh)^{n+1}_i = (rvh)^n_i - \frac{\Delta t}{A_i} \sum_{k=1}^{\text{NE}} (F_2 n_y + F_3 n_x)_k^{\downarrow} l_k - \Delta t \left( \frac{\tau_f}{\rho_w} \frac{|rvh|}{|rhu|} + \frac{25}{4} \frac{\mu_p}{\rho_w} \frac{|rhu| rvh}{(rh)^2 h^2} \right)_i^{n+1} \quad (92c)$$

$$(h\phi')^{n+1}_i = (h\phi')^n_i - \frac{\Delta t}{A_i} \sum_{k=1}^{\text{NE}} (F_4)_k^{\downarrow} l_k \quad (92d)$$

where  $h_i^{n+1} = (rh)_i^{n+1} - (h\phi')_i^{n+1}$  and  $\tau_{f,i}^{n+1} = (\rho_i^{n+1} - \rho_w) g h_i^{n+1} \tan \delta_f$ . For the sake of clarity, from now on  $rh = (rh)_i^{n+1}$ ,  $h = h_i^{n+1}$  and  $\tau_f = \tau_{f,i}^{n+1}$  are used.

We define the cell quantities

$$\begin{aligned} (m_x)_i^{n+1} &= (rhu)_i^n - \frac{\Delta t}{A_i} \sum_{k=1}^{\text{NE}} (F_2 n_x - F_3 n_y)_k^{\downarrow} l_k \\ (m_y)_i^{n+1} &= (rvh)_i^n - \frac{\Delta t}{A_i} \sum_{k=1}^{\text{NE}} (F_2 n_y + F_3 n_x)_k^{\downarrow} l_k \end{aligned} \quad (93)$$

which represent the mass rate at the cells without including the basal resistance contributions, i.e. including only the conservative flux and the bed-pressure momentum contribution, updated at the time  $t^{n+1}$ .

Considering that the basal resistance term only can slow down the flow, we assume that

$$\begin{aligned} \text{sgn } (rhu)_i^{n+1} &= \text{sgn } (m_x)_i^{n+1} \\ \text{sgn } (rvh)_i^{n+1} &= \text{sgn } (m_y)_i^{n+1} \end{aligned} \quad (94)$$

Therefore, it is possible to write the momentum Eqs. (92b) and (92c) along the  $x$ - and  $y$ -coordinates, respectively, in terms of absolute values as

$$|rhu|_i^{n+1} = |m_x|_i^{n+1} - \Delta t \frac{\tau_f}{\rho_w} \frac{|rhu|_i^{n+1}}{|rhu|_i^{n+1}} - \Delta t \frac{25}{4} \frac{\mu_p}{\rho_w} \frac{|rhu|_i^{n+1} |rhu|_i^{n+1}}{(rh)^2 h^2} \quad (95)$$

$$|rvh|_i^{n+1} = |m_y|_i^{n+1} - \Delta t \frac{\tau_f}{\rho_w} \frac{|rvh|_i^{n+1}}{|rhu|_i^{n+1}} - \Delta t \frac{25}{4} \frac{\mu_p}{\rho_w} \frac{|rhu|_i^{n+1} |rvh|_i^{n+1}}{(rh)^2 h^2} \quad (96)$$

For the sake of simplicity, we replace  $\mathcal{Q}_x \equiv |rhu|_i^{n+1}$ ,  $\mathcal{Q}_y \equiv |rvh|_i^{n+1}$ ,  $\mathcal{M}_x \equiv |m_x|_i^{n+1}$  and  $\mathcal{M}_y \equiv |m_y|_i^{n+1}$ . Rearranging (95) and (96) allows to express

$$\mathcal{Q}_x \left( 1 + \Delta t \frac{\tau_f}{\rho_w} \frac{1}{\sqrt{\mathcal{Q}_x^2 + \mathcal{Q}_y^2}} + \Delta t \frac{25}{4} \frac{\mu_p}{\rho_w} \frac{\sqrt{\mathcal{Q}_x^2 + \mathcal{Q}_y^2}}{(rh)^2 h^2} \right) = \mathcal{M}_x \quad (97)$$

$$\mathcal{Q}_y \left( 1 + \Delta t \frac{\tau_f}{\rho_w} \frac{1}{\sqrt{\mathcal{Q}_x^2 + \mathcal{Q}_y^2}} + \Delta t \frac{25}{4} \frac{\mu_p}{\rho_w} \frac{\sqrt{\mathcal{Q}_x^2 + \mathcal{Q}_y^2}}{(rh)^2 h^2} \right) = \mathcal{M}_y \quad (98)$$

and dividing (97) by (98) leads to

$$\frac{\mathcal{Q}_x}{\mathcal{Q}_y} = \frac{\mathcal{M}_x}{\mathcal{M}_y} \quad (99)$$

Focusing on the momentum along the  $x$ -coordinate, replacing (99) into (97) allows us to express

$$\mathcal{Q}_x \left( 1 + \Delta t \frac{\tau_f}{\rho_w} \frac{1}{\mathcal{Q}_x \sqrt{1 + (\frac{\mathcal{M}_y}{\mathcal{M}_x})^2}} + \Delta t \frac{25}{4} \frac{\mu_p}{\rho_w} \frac{\mathcal{Q}_x \sqrt{1 + (\frac{\mathcal{M}_y}{\mathcal{M}_x})^2}}{(rh)^2 h^2} \right) = \mathcal{M}_x \quad (100)$$

and reordering (100) leads to

$$\frac{25}{4} \Delta t \frac{\mu_p}{\rho_w} \frac{\sqrt{1 + (\frac{\mathcal{M}_y}{\mathcal{M}_x})^2}}{(rh)^2 h^2} \mathcal{Q}_x^2 + \mathcal{Q}_x + \left( \frac{\Delta t \frac{\tau_f}{\rho_w}}{\sqrt{1 + (\frac{\mathcal{M}_y}{\mathcal{M}_x})^2}} - \mathcal{M}_x \right) = 0 \quad (101)$$

Therefore, (101) is a quadratic equation in terms of  $\mathcal{Q}_x$  with roots

$$\mathcal{Q}_x = \frac{-1 \pm \sqrt{1 - 25 \Delta t \frac{\mu_p}{\rho_w} (rh)^{-2} h^{-2} \sqrt{1 + (\frac{\mathcal{M}_y}{\mathcal{M}_x})^2} \left( \frac{\Delta t \frac{\tau_f}{\rho_w}}{\sqrt{1 + (\frac{\mathcal{M}_y}{\mathcal{M}_x})^2}} - \mathcal{M}_x \right)}}{\frac{25}{2} \Delta t \frac{\mu_p}{\rho_w} (rh)^{-2} h^{-2} \sqrt{1 + (\frac{\mathcal{M}_y}{\mathcal{M}_x})^2}} \quad (102)$$

The unique real solution that satisfies positivity is

$$\mathcal{Q}_x = \frac{-1 + \sqrt{1 - 25 \Delta t \frac{\mu_p}{\rho_w} (rh)^{-2} h^{-2} \mathcal{M}_x^{-1} \sqrt{\mathcal{M}_x^2 + \mathcal{M}_y^2} \left( \frac{\mathcal{M}_x \Delta t \frac{\tau_f}{\rho_w}}{\sqrt{\mathcal{M}_x^2 + \mathcal{M}_y^2}} - \mathcal{M}_x \right)}}{\frac{25}{2} \Delta t \frac{\mu_p}{\rho_w} (rh)^{-2} h^{-2} \mathcal{M}_x^{-1} \sqrt{\mathcal{M}_x^2 + \mathcal{M}_y^2}} \quad (103)$$

Reordering (103) leads to

$$\mathcal{Q}_x = \frac{-1 + \sqrt{1 + 25 \Delta t \frac{\mu_p}{\rho_w} (rh)^{-2} h^{-2} \left( \sqrt{\mathcal{M}_x^2 + \mathcal{M}_y^2} - \Delta t \frac{\tau_f}{\rho_w} \right)}}{\frac{25}{2} \Delta t \frac{\mu_p}{\rho_w} (rh)^{-2} h^{-2} \sqrt{\mathcal{M}_x^2 + \mathcal{M}_y^2}} \mathcal{M}_x \quad (104)$$

which only ensures non-negativity if satisfies

$$\tau_f \leq \frac{\rho_w}{\Delta t} \sqrt{\mathcal{M}_x^2 + \mathcal{M}_y^2} \quad (105)$$

If  $\tau_f > \rho_w \sqrt{\mathcal{M}_x^2 + \mathcal{M}_y^2} / \Delta t$  the yield stress contribution in (104) is larger than the frictionless momentum and hence the updated mass rate  $\mathcal{Q}_x$  would be null.

This derivation is straightforward applicable to the mass rate  $\mathcal{Q}_y$  evolution along the  $y$ -coordinate. Therefore, the updated mass rate along the  $x$ - and  $y$ -coordinates can be rewritten as

$$(rhu)_i^{n+1} = \mathcal{T}_i (m_x)_i^{n+1} \\ (rvu)_i^{n+1} = \mathcal{T}_i (m_y)_i^{n+1} \quad (106)$$

being  $\mathcal{T}_i$  the implicit basal resistance factor defined as

$$\mathcal{T}_i = \frac{-1 + \sqrt{1 + 25 \Delta t \frac{\mu_p}{\rho_w} (rh)^{-2} h^{-2} \left( \sqrt{\mathcal{M}_x^2 + \mathcal{M}_y^2} - \Delta t \frac{\tau_f}{\rho_w} \right)}}{\frac{25}{2} \Delta t \frac{\mu_p}{\rho_w} (rh)^{-2} h^{-2} \sqrt{\mathcal{M}_x^2 + \mathcal{M}_y^2}} \quad (107)$$

In order that the basal resistance contribution does not accelerate the flow, the implicit basal resistance factor must also satisfies  $\mathcal{T}_i \leq 1$ .

## References

- Armanini, A., Fraccarollo, L., Rosatti, G., 2009. Two-dimensional simulation of debris flows in erodible channels. *Comput. Geosci.* 35 (5), 993–1006.  
 Brufau, P., García-Navarro, P., Ghilardi, P., Natale, L., Savi, F., 2000. 1D Mathematical modelling of debris flow. *J. Hydraulic Res.* 38 (6), 435–446.

- Burguete, J., García-Navarro, P., Murillo, J., 2008. Friction term discretization and limitation to preserve stability and conservation in the 1D shallow-water model: application to unsteady irrigation and river flow. *Int. J. Numer. Meth. Fluids* 54, 403–425.  
 Castro, M., Fernández-Nieto, E., Ferreiro, A., García-Rodríguez, J., Parés, C., 2009. High order extensions of ROE schemes for two-dimensional nonconservative hyperbolic systems. *J. Sci. Comput.* 39, 67–114.

- Cea, L., Bladé, E., 2015. A simple and efficient unstructured finite volume scheme for solving the shallow water equations in overland flow applications. *Water Resour. Res.* 51 (7), 5464–5486.
- Coulomb, C., 1773. Sur une application des règles de maximis et minimis à quelques problèmes de statique, relatifs à l'architecture. *Memires De Mathemat. Phys.* 7, 343–382.
- Cozzolino, L., Varra, G., Cimorelli, L., Pianese, D., Della Morte, R., 2021. Friction decoupling and loss of rotational invariance in 2D flooding models. *Adv. Water Res.* 152, 103919.
- George, D.L., Iverson, R.M., 2014. A depth-averaged debris-flow model that includes the effects of evolving dilatancy. II. Numerical predictions and experimental tests. *Proc. Royal Soc.: Mathemat. Phys. Eng. Sci.* 470 (2170), 20130820.
- Godlewski, E., Raviart, P.A., 1996a. Numerical Approximation of Hyperbolic Systems of Conservation Laws. Springer-Verlag, New York.
- Godlewski, E., Raviart, P.A., 1996b. Numerical Approximation of Hyperbolic Systems of Conservation Laws. Springer-Verlag, New York.
- Hungr, O., 1995. A model for the runout analysis of rapid flow slides, debris flows, and avalanches. *Can. Geotech. J.* 32 (4), 610–623.
- Iverson, R.M., Vallance, J.W., 2001. New views of granular mass flows. *Geology* 29 (2), 115–118.
- Iverson, R.M., Logan, M., LaHusen, R.G., Berti, M., 2010. The perfect debris flow? Aggregated results from 28 large-scale experiments. *J. Geophys. Res.: Earth Surf.* 115, F03005.
- Iverson, R.M., Reid, M.E., Logan, M., LaHusen, R.G., Godt, J.W., Griswold, J.P., 2011. Positive feedback and momentum growth during debris-flow entrainment of wet bed sediment. *Nat. Geosci.* 4, 116–121.
- Jakob, M., Hungr, O., 2005. Debris-flow Hazards and Related Phenomena, Springer Praxis Books. Springer, Berlin Heidelberg.
- Juez, C., Murillo, J., García-Navarro, P., 2013. 2D simulation of granular flow over irregular steep slopes using global and local coordinates. *J. Comput. Phys.* 255, 166–204.
- Juez, C., Caviedes-Voullième, D., Murillo, J., García-Navarro, P., 2014. 2D dry granular free-surface transient flow over complex topography with obstacles. Part II: numerical predictions of fluid structures and benchmarking. *Comput. Geosci.* 73, 142–163.
- Lancaster, S.T., Hayes, S.K., Grant, G.E., 2003. Effects of wood on debris flow runout in small mountain watersheds. *Water Resour. Res.* 39 (6), 21.
- Li, J., Cao, Z., Hu, K., Pender, G., Liu, Q., 2018. A depth-averaged two-phase model for debris flows over erodible beds. *Earth Surf. Process. Landforms* 43 (4), 817–839.
- Luna, B.Q., Remaître, A., [van Asch], T., Malet, J.-P., [van Westen], C., 2012. Analysis of debris flow behavior with a one dimensional run-out model incorporating entrainment. *Eng. Geol.* 128, 63–75.
- Martínez-Aranda, S., Murillo, J., García-Navarro, P., 2020. A robust two-dimensional model for highly sediment-laden unsteady flows of variable density over movable beds. *J. Hydroinf.* 22 (5), 1138–1160.
- Murillo, J., García-Navarro, P., 2010. Weak solutions for partial differential equations with source terms: application to the shallow water equations. *J. Comput. Phys.* 229, 4327–4368.
- Murillo, J., García-Navarro, P., 2012. Wave Riemann description of friction terms in unsteady shallow flows: application to water and mud/debris floods. *J. Comput. Phys.* 231, 1963–2001.
- Murillo, J., Navas-Montilla, A., 2016. A comprehensive explanation and exercise of the source terms in hyperbolic systems using ROE type solutions. Application to the 1D-2D shallow water equations. *Adv. Water Res.* 98, 70–96.
- Murillo, J., García-Navarro, P., Burguete, J., 2008. Time step restrictions for well balanced shallow water solutions in non-zero velocity steady states. *Int. J. Numer. Meth. Fluids* 56, 661–686.
- Martínez-Aranda, S., 2021. Efficient Simulation Tools (EST) for sediment transport in geomorphological shallow flows, Ph.D. thesis. Universit of Zaragoza, Spain.
- Martínez-Aranda, S., Murillo, J., García-Navarro, P., 2021. A GPU-accelerated Efficient Simulation Tool (EST) for 2D variable-density mud/debris flows over non-uniform erodible beds. *Eng. Geol.* 296, 106462.
- Martínez-Aranda, S., Fernández-Pato, J., Echeverriar, I., Navas-Montilla, A., Morales-Hernández, M., Brufau, P., Murillo, J., García-Navarro, P., 2021. Finite volume models and efficient simulation tools (EST) for shallow flows. *Advances in Fluid Mechanics: Modelling and Simulations*. Springer Nature, Switzerland AG.
- Naef, D., Rickenmann, D., Rutschmann, P., Mcardell, B.W., 2006. Comparison of flow resistance relations for debris flows using a one-dimensional finite element simulation model. *Nat. Hazards Earth Syst. Sci.* 6 (1), 155–165.
- Ouyang, C., He, S., Xu, Q., 2015. MacCormack-TVD finite difference solution for dam break hydraulics over erodible sediment beds. *J. Hydraulic Eng.* 141 (5), 06014026.
- Pastor, M., Blanc, T., Haddad, B., Drempetic, V., Sanchez-Morles, M., Dutto, P., Martin-Stickle, M., Mira, P., Fernández-Merodo, J., 2015. Depth averaged models for fast landslide propagation: mathematical, rheological and numerical aspects. *Archives Computat. Methods Eng.* 22, 67–104.
- Pirulli, M., Bristeau, M.-O., Mangeney, A., Scavia, C., 2007. The effect of the earth pressure coefficients on the runout of granular material. *Environ. Modell. Software* 22 (10), 1437–1454.
- Quecedo, M., Pastor, M., Herreros, M.I., Fernández Merodo, J.A., 2004. Numerical modelling of the propagation of fast landslides using the finite element method. *Int. J. Num. Methods Eng.* 59 (6), 755–794.
- Rosatti, G., Murillo, J., Fraccarollo, L., 2008. Generalized ROE schemes for 1D two-phase, free-surface flows over a mobile bed. *J. Comput. Phys.* 227, 10058–10077.
- Terzaghi, K., 1936. The shearing resistance of saturated soils and the angle between the planes of shear. *Proced. 1st Int. Conf. Soil Mech. Found. Eng.* 1, 54–56.
- Toro, E., 1997. Riemann Solvers and Numerical Methods for Fluid Dynamics: A Practical Introduction. Springer-Verlag, Berlin Germany.
- Xia, X., Liang, Q., 2018. A new efficient implicit scheme for discretising the stiff friction terms in the shallow water equations. *Adv. Water Res.* 117, 87–97.
- Xia, X., Liang, Q., Ming, X., Hou, J., 2017. An efficient and stable hydrodynamic model with novel source term discretization schemes for overland flow and flood simulations. *Water Resour. Res.* 53 (5), 3730–3759.
- Xia, C., Li, J., Cao, Z., Liu, Q., Hu, K., 2018. A quasi single-phase model for debris flows and its comparison with a two-phase model. *J. Mountain Sci.* 15 (5), 1071–1089.